Neutron Form Factors from Quasi-Elastic Electron-Deuteron Scattering*†

R. J. BUDNITZ,‡ J. APPEL,§ L. CARROLL,‖ J. CHEN, J. R. DUNNING, JR., M. GOITEIN,**
K. HANSON, D. IMRIE,†† C. MISTRETTA, J. K. WALKER, AND RICHARD WILSON
Harvard University, Cambridge, Massachusetts 02138
(Received 29 February 1968)

The differential cross section for quasi-elastic electron-deuteron scattering has been measured at the Cambridge Electron Accelerator in the four-momentum-transfer region from 7 to 115 F^{-2} f[0.27 to 4.47 $(BeV/c)^2$]. The method used involved a coincidence between scattered electrons and recoiling protons. Electrons without a high-energy proton in coincidence were assumed to be due to a neutron interaction. The impulse approximation as developed by Durand and McGee was used to extract from the data the ratio of neutron to proton cross sections. Neutron/proton cross-section ratios from deuterium were measured at $q^2=7$, 10, 15, 20, 30, 45, and 70 F^{-2} (at 20°); at $q^2=15$ F^{-2} (at 90°); and at $q^2=115$ F^{-2} (at 29.64°). It is shown that in the low-q^2 region there are problems of theoretical interpretation. Finally, all available experimental data on the electron-neutron interaction are used to calculate values for the neutron form factors.

I. INTRODUCTION

THIS paper reports measurements of the differential cross sections of electrons scattered quasi-elastically from deuterons. At a laboratory angle of 20°, the square of the four-momentum transfer to the nucleon (q^2) was varied from 7 to 70 F^{-2}. At $q^2=15$ F^{-2}, a measurement was made at 90° as well as at 20°, and at $q^2=115$ F^{-2}, a 29.64° measurement was taken. The external electron beam from the Cambridge Electron Accelerator was used. Electrons were detected in a quadrupole magnet spectrometer and recoiling protons were detected in a counter telescope. The layout of the apparatus is shown schematically in Fig. 1.

The cross section for scattering of electrons from free neutrons was derived from the actual measurements using the impulse approximation in a form calculated by Durand[1,2] and McGee.[3,4] The aim of the experiment was to measure explicitly the *ratio* of neutron to proton scattering cross sections from deuterium. As discussed below, this ratio (called σ_n/σ_p) is significantly less sensitive to several known sources of error than would be any absolute cross-section measurement.

Electron-neutron scattering cross sections were also obtained using the area under the quasi-elastic electron momentum spectrum.

At each measurement taken at 20°, elastic electron-proton scattering cross sections from liquid hydrogen were also measured. Preliminary reports have already been given of some of the hydrogen[5] and deuterium[6] data.

The kinematic quantities associated with each datum point are listed in Table I. Section II describes the relation of this work to earlier measurements. The deuteron theory used is outlined in Sec. III. Sections IV–VIII contain descriptions of the experimental technique and the data analysis. The results of the present experiment are contained in Secs. IX–XIII. Section XIV discusses the available data on the electron-neutron interaction and our present knowledge of the neutron form factors.

II. EARLIER MEASUREMENTS

There are three methods which have been used in the past to measure neutron electromagnetic form factors:

(a) neutron scattering from high-Z elements at extremely low energies;

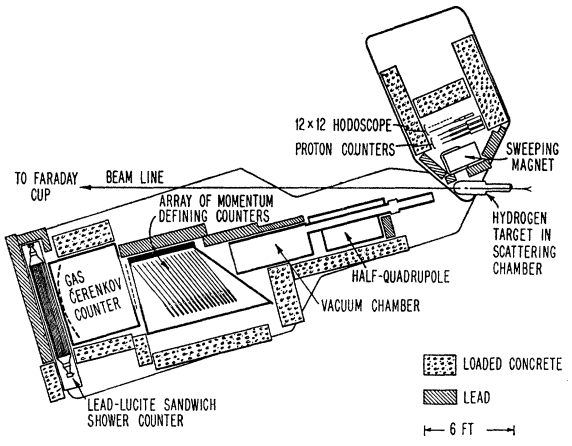

FIG. 1. Schematic plan—view of the apparatus.

* Work supported by the U. S. Atomic Energy Commission.
† A more complete account can be found in the Ph.D. thesis of R. J. Budnitz, Harvard University, 1967 (unpublished).
‡ Presently at the Lawrence Radiation Laboratory, University of California, Berkeley, California.
§ Danforth Foundation Graduate Fellow.
‖ Presently at Liverpool University, Liverpool, England.
** Partially supported by a Frank Knox Fellowship and by an I.B.M. Fellowship.
†† On leave from University College London, London, England.
[1] L. Durand, Phys. Rev. **115**, 1020 (1959).
[2] L. Durand, Phys. Rev. **123**, 1393 (1961).
[3] I. McGee, Ph.D. thesis, Yale University, 1965 (unpublished).
[4] I. McGee, Phys. Rev. **158**, 1500 (1967); **161**, 1640 (1967).
[5] M. Goitein, R. J. Budnitz, L. Carroll, J. Chen, J. R. Dunning, Jr., K. Hanson, D. Imrie, C. Mistretta, J. K. Walker, Richard Wilson, G. F. Dell, M. Fotino, J. M. Paterson, and H. Winick, Phys. Rev. Letters **18**, 1016 (1967).
[6] R. Budnitz, J. Appel, L. Carroll, J. Chen, J. R. Dunning, Jr., M. Goitein, K. Hanson, D. Imrie, C. Mistretta, J. K. Walker, and Richard Wilson, Phys. Rev. Letters **19**, 809 (1967).

TABLE I. Kinematic parameters of the measured data points.

				← Parameters for elastic scattering →			
q^2 (F^{-2})	q^2 (BeV/c)^2	θ electron angle	E_0 incident e^- energy (BeV)	E' scattered e^- energy (BeV)	ϕ proton angle	T_p' proton energy (BeV)	p_p' proton momentum (BeV/c)
7	0.272	20°	1.578	1.433	64.69°	0.145	0.542
10	0.389	20°	1.904	1.696	61.89°	0.208	0.658
15	0.583	20°	2.362	2.051	58.19°	0.311	0.825
20	0.778	20°	2.758	2.342	55.22°	0.415	0.975
30	1.167	20°	3.440	2.817	50.55°	0.623	1.248
45	1.751	20°	4.308	3.374	45.41°	0.934	1.620
70	2.723	20.16°	5.500	4.047	39.35°	1.453	2.200
115	4.473	29.64°	5.500	3.113	28.85°	2.387	3.191
15	0.583	90°	0.718	0.407	29.53°	0.311	0.825

(b) elastic electron-deuteron scattering;
(c) quasi-elastic electron-deuteron scattering. The experiment reported here falls into category (c).

(a) Beginning with the work of Fermi and Marshall,[7] several measurements[8–10] involving neutrons scattered from high-Z elements have been made.

The most accurate data are now the scattering measurements with noble gases by Krohn and Ringo,[8] who find

$$\left.\frac{d(G_{En})}{dq^2}\right|_{q^2\to 0} = 0.018 \pm 0.001 \text{ F}^2. \quad (1)$$

(b) Elastic electron-deuteron scattering experiments[11] at forward scattering angles can be used to measure the quantity $G_E = G_{Ed}\ (G_{En}+G_{Ep})$, but the coherent-deuteron form factor G_{Ed} must unfortunately be calculated theoretically.

Despite difficult theoretical problems involved in the calculations of the deuteron form factors, much effort has gone into attempts to extract G_{En} from the data. Casper and Gross[11] apply relativistic corrections in a consistent manner. They find a slight difference between different deuteron wave functions which fit nucleon-nucleon scattering data; and using the new Lomon-Feshbach wave functions,[12] they have derived values of G_{En} from elastic e-d data which, for the first time, are consistent with the value of dG_{En}/dq^2 (at $q^2=0$) obtained from the low-energy neutron-electron interaction work.

(c) The third method which has been used to obtain electron-neutron cross sections is through quasi-elastic electron-deuteron scattering. Three different types of quasi-elastic experiments have been performed:

(i) those with electron detection only;
(ii) those with electron and neutron detection;
(iii) those with electron and proton detection.

(i) Measurements detecting electrons only have been carried out at Stanford,[13] Orsay,[14] Cornell,[15] and Harvard.[16] A naive expectation would be that an integration over the entire quasi-elastic peak (neglecting for the moment any radiative effects) would yield the total differential cross section:

$$\int dE'\left(\frac{d^2\sigma}{d\Omega dE'}\right) = \left(\frac{d\sigma}{d\Omega}\right)_{ep} + \left(\frac{d\sigma}{d\Omega}\right)_{en}. \quad (2)$$

The neutron term is particularly sensitive to any corrections to the integral, however, because the neutron/proton cross-section ratio is never found to be more than about $\frac{1}{2}$, and at low q^2 is even smaller. Thus, any direct corrections to (or uncertainties in) the integrated peak cross section are enhanced by factors of from 2 to 4 in their effect on the neutron cross section.

An analysis of the data using Eq. (2) is usually called "area-method" analysis. There are two main theoretical problems: the effect of the D state and the effect of final-state interactions. Some systematic experimental errors cancel, however, especially because the usual experimental procedure is a direct comparison with elastic electron-proton measurements from hydrogen:

$$\frac{\sigma_{e\mathrm{D}}}{\sigma_{e\mathrm{H}}} = \frac{(\sigma_p+\sigma_n)_D}{(\sigma_p)_{\mathrm{H}}} = \frac{\sigma_{p\mathrm{D}}}{\sigma_{p\mathrm{H}}} + \frac{\sigma_{n\mathrm{D}}}{\sigma_{p\mathrm{H}}} \approx 1 + \frac{\sigma_n}{\sigma_p}. \quad (3)$$

This comparison relies upon the assumption that bound and free nucleons scatter identically. In particular, we require

$$\sigma_{(\text{bound proton})} = \sigma_{(\text{free proton})}. \quad (4)$$

[7] E. Fermi and L. Marshall, Phys. Rev. **72**, 1139 (1947).
[8] V. Krohn and G. Ringo, Phys. Rev. **148**, 1303 (1966).
[9] E. Melkonian, B. Rustad, and W. W. Havens, Phys. Rev. **114**, 1571 (1959).
[10] D. Hughes, J. Harvey, M. Goldberg, and M. Stafne, Phys. Rev. **90**, 497 (1953).
[11] D. Drickey and L. Hand, Phys. Rev. Letters **9**, 521 (1962); D. Benaksas, D. Drickey, and D. Frerejacque, Phys. Rev. Letters **13**, 353 (1964). The above data have been reanalyzed by B. Casper and F. Gross, Phys. Rev. **155**, 1607 (1967).
[12] E. Lomon and H. Feshbach (private communication).
[13] E. B. Hughes, T. A. Griffy, M. R. Yearian, and R. Hofstadter, Phys. Rev. **139**, B458 (1965); **146**, 973 (1966).
[14] B. Grossetête, S. Jullian, and P. Lehmann, Phys. Rev. **141**, 1435 (1966).
[15] C. Akerlof, K. Berkelman, G. Rouse, and M. Tigner, Phys. Rev. **135**, B810 (1964).
[16] J. R. Dunning Jr., K. W. Chen, A. Cone, G. Hartwig, N. Ramsey, J. Walker, and R. Wilson, Phys. Rev. **141**, 1286 (1966).

There is no way of checking the validity of this assumption in the noncoincidence measurements, and the ability to do so is a crucial point in favor of the coincidence experiments, one type of which is the subject of this paper. A significant variation of the noncoincidence technique is the comparison with theory of the doubly differential cross section at the top of the quasi-elastic peak. In the language of pole models, one is closest to the nucleon pole at the top of the peak, and closest to the (unphysical) point where the theory is exact. Calculations using pole models, such as those of Durand,[1,2] suggest that the cross section at the top of the peak may be significantly less sensitive to deuteron-model and final-state interaction effects than is the entire integrated cross section. It is not, however, clear whether or not sum rules might show that Eq. (2) is more accurate than the pole-model method, for different reasons. The data reported in this paper suggest that this might be the case. Analysis of the data in this way is called "peak-method" analysis, in contrast to the "area method" of integrating over the entire peak. In the peak method, one requires a very good knowledge of the momentum resolution and of the experimental momentum acceptance.

(ii) The neutron-coincidence method, employed at Cornell,[17] involves the detection of a recoiling neutron in coincidence with the scattered electron. The statistical problem with the subtraction of two large numbers is avoided, but in its place are introduced two other problems: the reduced statistical precision resulting from the rather low efficiency of the neutron-detecting counter, and uncertainties in the absolute counter efficiency. This method is relatively unattractive only because of the low statistical accuracy obtainable.

(iii) The last category of quasi-elastic experiment, into which the data reported here fall, employs a proton-detecting telescope to measure coincidences between scattered electrons and recoiling high-energy protons. Any electron which does *not* have a proton in coincidence is attributed to scattering from the neutron. This will be called the "anticoincidence" method.

What is actually measured is the ratio:

$$\frac{(\text{electrons with } p \text{ coincidence})}{(\text{all electrons})}=\frac{\sigma_{ep}}{\sigma_{\text{all}\,e}}=\frac{\sigma_{ep}}{\sigma_{ep}+\sigma_{en}}. \quad (5)$$

This method exploits several advantages: better statistical precision, partial cancellation of deuteron-model and final-state interaction effects, and the ability to study the σ_n/σ_p ratio across the quasi-elastic peak. However, the most important *experimental* advantage is that the entire system can be studied (and calibrated) by doing the elastic hydrogen measurement corresponding to the same kinematic situation. The proton-counter efficiencies can be studied and set; the electron-detection apparatus can be calibrated; and the hydrogen data can be used as an absolute standard, to which the more difficult deuterium measurements can be compared for the purposes of extracting absolute deuterium cross sections. In addition, a comparison of free-proton (hydrogen) to bound-proton (deuterium) cross section enables one to check and possibly resolve some of the aspects and problems involved in the deuteron-model-dependent assumptions.

The corrections to the raw data are few. In addition to the conceptually simple chance-rate and target end-wall corrections, the most important corrections involve the efficiency of the proton counters, and the fact that some of the protons are missed because the kinematic smearing throws them out of the solid angle accepted by the counters.

Both the counter-efficiency and target end-wall corrections can be studied experimentally. The hydrogen measurements taken in conjunction with the deuterium data enable the ratio $(e+p)/(\text{all } e)$ to be determined for protons and electrons of essentially the same momenta as those in the deuterium measurements. The electrons without coincidences from hydrogen should come from and be entirely accounted for by only two sources: from the target-wall scattering (measured by a data run with an empty target cup), and from the process of proton nuclear absorption in the target, air, and counters. The measurement of the nuclear absorption effect can then be carried over directly and applied to the deuterium data. Also, a successful calculation of the size of the observed effect gives additional confidence in the correction for neutron conversion, which also occurs in the deuterium data and which must be calculated from *n*-lead, *n*-carbon, and *n-p* data.

In addition, rate-dependent, counter-efficiency and discrimination-level studies can be performed on hydrogen, to study the efficiency of the proton-counter telescope. Another correction to the raw data is due to the fact that some high-energy protons are not detected because they are thrown outside of the telescope, by the tails of the deuteron momentum-space wave function. This problem can be studied by using a counter hodoscope to measure the angular distribution of recoiling protons. A check against the theory can then help to place limits on the fraction of protons which could have escaped detection. The presence of final-state interactions might also throw protons outside of the telescope. Theoretical estimates by Durand[1,2] suggest that this effect should be small.

III. THEORY

We define the following quantities, where the asterisk (*) denotes quantities in the center-of-mass (c.m.) system of the final neutron and proton. All other quantities are in the laboratory frame.

$\mathbf{q}^2=\mathbf{q}_v\cdot\mathbf{q}_v-q_0q_0=$ invariant four-momentum transfer squared,

[17] P. Stein, M. Binkley, R. McAllister, A. Suri, and W. Woodward, Phys. Rev. Letters **16**, 592 (1966).

$q_0,\mathbf{q}_v$ = laboratory energy transfer, three-momentum transfer,
M = mean nucleon mass,
ϵ = binding energy of deuteron ($\epsilon>0$),
$\tau=(q^2/4M^2)$,
$\alpha=(2M\epsilon)^{1/2}$,
θ,ϕ = electron, proton laboratory scattering angles,
$d\Omega$ = electron scattered solid angle,
E,E' = incident, scattered-electron laboratory energies,
E'_{peak} = E'(lab) at top of quasi-elastic peak,
ω,ω^* = proton angle, measured from q direction, in laboratory and in n-p c.m. system,
W^* = total c.m. energy of both nucleons,
$\mathbf{p}^*$ = c.m. momentum of either nucleon,
$q_0^*,\mathbf{q}^*$ = c.m. timelike and spacelike components of q^μ,
$\mathbf{p}_p,\mathbf{p}_n$ = proton and neutron final laboratory momenta.

A. Impulse Approximation

The elastic scattering of electrons by free nucleons was first described using the Born approximation by Rosenbluth.[18] The form used in most recent descriptions of e-p and e-n data was first written down by Barnes,[19] and by Hand, Miller, and Wilson[20]:

$$d\sigma/d\Omega=(d\sigma/d\Omega)_{\text{Mott}}(E'/E)[A(\theta,q^2)G_E^2(q^2)+B(\theta,q^2)G_M^2(q^2)], \quad (6)$$

where

$$A=1/(1+\tau),\qquad B=\tau/(1+\tau)+2\tau\tan^2(\tfrac{1}{2}\theta). \quad (7)$$

In considering the situation in which electrons scatter quasi-elastically from deuterons, one could begin with the naive assumption that the deuteron consists of a proton and a neutron which are completely unbound. The cross section for electron scattering would then be written as in Eq. (2).

However, we know that the deuteron *is* bound; in fact, there is much information[21] about the wave function which describes the bound state. A slightly more realistic assumption, therefore, might be that the only effect of the deuteron binding on the scattering reaction is the introduction of the "moving target."

This second-level approximation is known as the *impulse approximation*. Since in the slightly smeared kinematics, the electrons no longer have a unique final momentum, the scattered electron spectrum (now known as *quasi-elastic*) must be described by a cross section differential in scattered energy as well as in electron solid angle. Such a description was first discussed in detail by Jankus[22] and Goldberg[23] and more recently by Durand[1,2] and McGee.[3,4] The momenta of the protons and neutrons emerging from such a scattering process would also be smeared out by the wave function. Indeed, the *triply* differential cross section (differential now in the angle of the recoiling proton) must be written in a form which takes this effect into account.

Now, one should expect, in the approximation where the only effect of the deuteron binding is to smear out the kinematics, that the amount of the smearing (both the size of the nucleon angular cone, and the width in momentum space of the scattered-electron peak) would be directly determined by the square of the momentum-space deuteron wave function, with no other corrections. That expectation is roughly, but not exactly, true. One way of stating the aim of the deuteron theory, in fact, is precisely to say that it is *the determination of the extent to which the expectation is true*, and *the calculation of the corrections to it*.

B. Triply Differential Cross Section

The theoretical treatment used in the analyses of the data presented here is that of Durand[1,2] and McGee.[3,4] Although these authors have included a treatment of the effect of final-state interactions, they have been neglected in this analysis. McGee[3] has written down a nucleon current containing several small relativistic "correction terms," which have only been calculated to first order. Here, what is meant by "first order" is that a nonrelativistic expansion of the nucleon initial and final energies has been made:

$$E=(M^2+p^2)^{1/2}=M(1+p^2/2M^2+\cdots). \quad (8)$$

Only the first term, $p^2/2M^2$, is kept, while higher terms are dropped.

Before the cross section is written down we shall state here, for completeness, the relations between the Dirac and Pauli form factors (F_1 and F_2) and the more usual electric and magnetic form factors (G_E and G_M):

$$G_E=F_1-\tau\kappa F_2, \quad (9.1)$$

$$G_M=F_1+\kappa F_2. \quad (9.2)$$

Let us define the following integrals, which are written as functions of ω^* but which are actually only functions of $|\mathbf{p}^*-\frac{1}{2}\mathbf{q}^*|$:

$$F(\omega^*)=\int R^2dR\frac{u(R)}{R}j_0(|\mathbf{p}^*-\tfrac{1}{2}\mathbf{q}^*|R), \quad (10.1)$$

$$G(\omega^*)=\int R^2dR\frac{w(R)}{R}j_2(|\mathbf{p}^*-\tfrac{1}{2}\mathbf{q}^*|R), \quad (10.2)$$

$$F'(\omega^*)=\frac{\sin\omega^*}{2|\mathbf{p}^*-\frac{1}{2}\mathbf{q}^*|}\int j_1(|\mathbf{p}^*-\tfrac{1}{2}\mathbf{q}^*|R)\times\left[\frac{d}{dR}\left(\frac{u(R)}{R}\right)\right]R^2dR$$
$$=-\tfrac{1}{2}\sin\omega^*F(\omega^*), \quad (10.3)$$

[18] M. N. Rosenbluth, Phys. Rev. **79**, 615 (1950).
[19] K. J. Barnes, Phys. Letters **1**, 166 (1962).
[20] L. Hand, D. Miller, and R. Wilson, Rev. Mod. Phys. **35**, 335 (1963).
[21] Richard Wilson, *The Nucleon-Nucleon Interaction* (John Wiley & Sons, New York, 1963).
[22] V. Z. Jankus, Phys. Rev. **102**, 1586 (1956).
[23] A. Goldberg, Phys. Rev. **112**, 618 (1958).

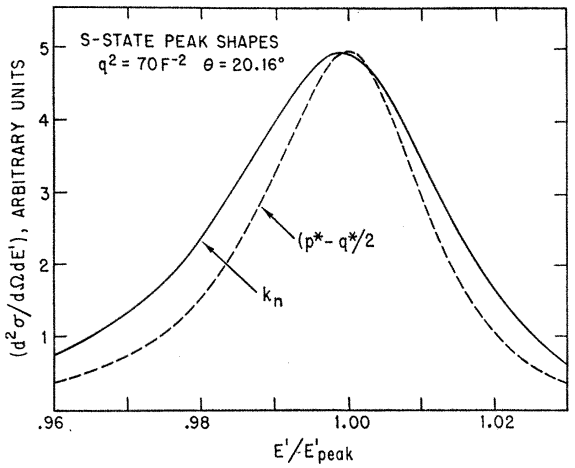

FIG. 2. S-state peak shapes at $q^2=70$ F^{-2}, $\theta=20°$ for ($\mathbf{k}_n$) and ($\mathbf{p}^*-\frac{1}{2}\mathbf{q}^*$) theories.

$$F''(\omega^*)=\int (1/q^2)j_0(|\mathbf{p}^*-\tfrac{1}{2}\mathbf{q}^*|R)\times\left[\frac{d^2}{dR^2}(u(R))\right]RdR. \quad (10.4)$$

Here, the j's are spherical Bessel functions and $u(R)$ and $w(R)$ are the S- and D-state parts of the deuteron radial wave function.

The triply differential cross section itself, taken from McGee's work[3,4] (but with some modifications due to Durand[1,2]) is written as

$$\frac{d^3\sigma}{d\Omega_e dE' d(\cos\omega^*)}=\left(\frac{d\sigma}{d\Omega}\right)_{\text{Mott}}\left(\frac{M_P M_N|\mathbf{p}^*|}{\pi W^*}\right)\times\sum_i \Lambda_i(\theta,q^2,\omega^*). \quad (11.1)$$

The various terms Λ_i are:

Ordinary S-state "big" terms:

$$\Lambda_{pp}{}^{SS}=(AG_{Ep}{}^2+BG_{Mp}{}^2)F^2(\omega^*), \quad (11.2)$$

$$\Lambda_{nn}{}^{SS}=(AG_{En}{}^2+BG_{Mn}{}^2)F^2(\pi-\omega^*). \quad (11.3)$$

Ordinary D-state "big" terms:

$$\Lambda_{pp}{}^{DD}=(AG_{Ep}{}^2+BG_{Mp}{}^2)G^2(\omega^*), \quad (11.4)$$

$$\Lambda_{nn}{}^{DD}=(AG_{En}{}^2+BG_{Mn}{}^2)G^2(\pi-\omega^*). \quad (11.5)$$

S-state n-p interference term:

$$\Lambda_{np}{}^{SS}=\{\tfrac{2}{3}\tau[2\tan^2(\tfrac{1}{2}\theta)+1]G_{Mp}G_{Mn}+2G_{Ep}G_{En}\}\times F(\omega^*)F(\pi-\omega^*). \quad (11.6)$$

D-state n-p interference term:

$$\Lambda_{np}{}^{DD}=\{(1/4M^2)[2\tan^2(\tfrac{1}{2}\theta)+1](G_{Mp}G_{Mn})\times[2q^2-\tfrac{3}{2}(Mq_0+\tfrac{3}{2}q^2)(\hat{p}_n\times\hat{p}_r)^2]+G_{Ep}G_{En}\times[3(\hat{p}_p\cdot\hat{p}_n)^2-1]\}G(\omega^*)G(\pi-\omega^*). \quad (11.7)$$

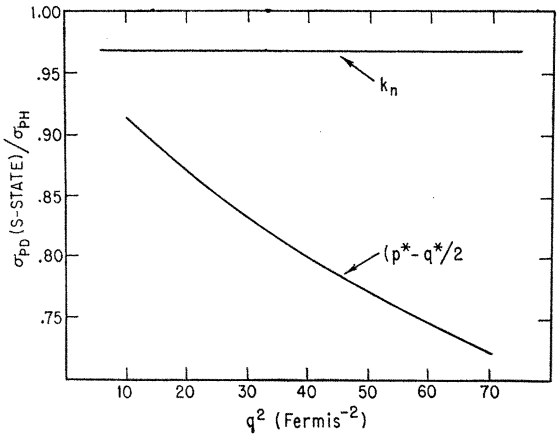

FIG. 3. Ratio of S-state proton cross sections to hydrogen for ($\mathbf{k}_n$) and ($\mathbf{p}^*-\frac{1}{2}\mathbf{q}^*$) theories, assuming 95% S-state probability.

S-D-state n-p interference term:

$$\Lambda_{np}{}^{SD}=(\sqrt{2}/6M^2)[2\tan^2(\tfrac{1}{2}\theta)+1](G_{Mp}G_{Mn})\times\{[q^2-\tfrac{3}{2}p_n{}^2(\hat{p}_p\times\hat{p}_n)^2]F(\omega^*)G(\pi-\omega^*)+[q^2-\tfrac{3}{2}p_p{}^2(\hat{p}_p\times\hat{p}_n)^2]G(\omega^*)F(\pi-\omega^*)\}. \quad (11.8)$$

S-State convection current terms:

$$\Lambda_{pp}{}^{\text{conv}}=\tau[2\tan^2(\tfrac{1}{2}\theta)+1]F_{1p}{}^2[F'(\omega^*)]^2, \quad (11.9)$$

$$\Lambda_{nn}{}^{\text{conv}}=\tau[2\tan^2(\tfrac{1}{2}\theta)+1]F_{1n}{}^2[F'(\pi-\omega^*)]^2, \quad (11.10)$$

$$\Lambda_{np}{}^{\text{conv}}=2\tau[2\tan^2(\tfrac{1}{2}\theta)+1]F_{1p}F_{1n}\times[F'(\omega^*)F'(\pi-\omega^*)]. \quad (11.11)$$

S-State double-derivative terms:

$$\Lambda_{pp}{}^{\text{deriv}}=-4\tau F_{1p}{}^2[F(\omega^*)F''(\omega^*)], \quad (11.12)$$

$$\Lambda_{nn}{}^{\text{deriv}}=-4\tau F_{1n}{}^2[F(\pi-\omega^*)F''(\pi-\omega^*)], \quad (11.13)$$

$$\Lambda_{np}{}^{\text{deriv}}=-4\tau F_{1p}F_{1n}[F(\omega^*)F''(\pi-\omega^*)+F(\pi-\omega^*)F''(\omega^*)]. \quad (11.14)$$

Durand has suggested[24] that the quantity $|\mathbf{p}^*-\frac{1}{2}\mathbf{q}^*|$ in the above expression should be replaced by the *neutron laboratory final momentum*, which we will call $\mathbf{k}_n$. The substitution is made to produce a better quasi-elastic peak shape at high momentum transfer. The two are completely identical in the nonrelativistic limit. At higher momentum transfers, this nonrelativistic limit is no longer correct, although even there it is very close to being true for electrons at the top of the quasi-elastic peak (where the final neutron is approximately at rest in the laboratory anyway).

Durand's suggestion can be tested experimentally, because the two forms of the theory make very different predictions about the quasi-elastic peak shape at the higher momentum transfers, and also about the total integrated electron cross section, summing over all E' values across the peak. Figure 2 shows the differences in the predicted S-state electron spectra at $q^2=70$ F^{-2},

[24] See Ref. 1, Eqs. (1)–(6).

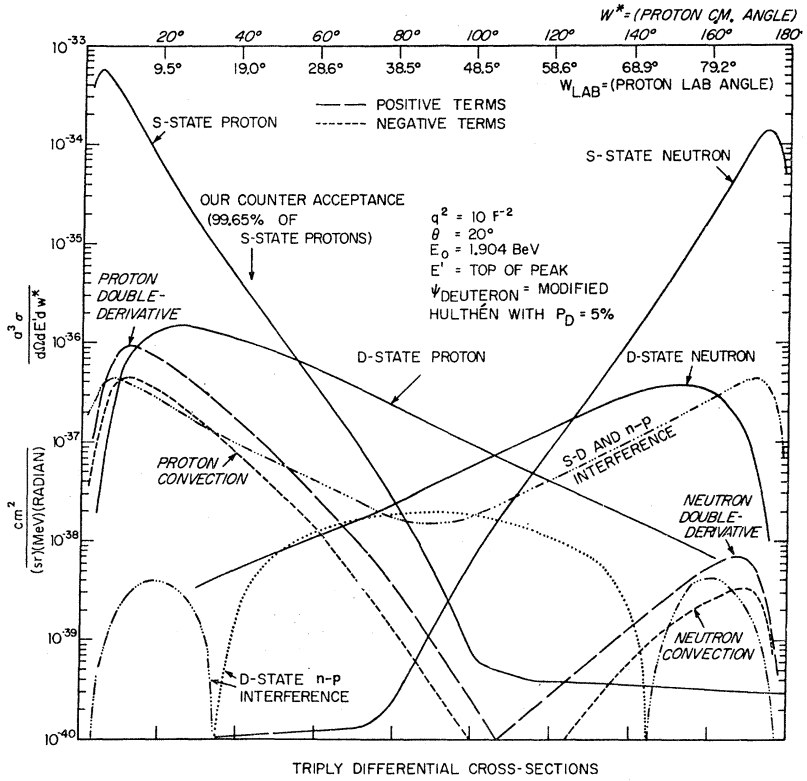

FIG. 4. Triply differential cross sections at $q^2=10$ F^{-2}, $\theta=20°$, showing different contributions.

while Fig. 3 shows the ratio of the total integrated proton S-state cross section (called σ_{pD}) to that for hydrogen elastic scattering, for various q^2 in our range. The $|\mathbf{p}^*-\frac{1}{2}\mathbf{q}^*|$ theory predicts that the deuterium cross section is increasingly smaller than the hydrogen value as q^2 increases. Our experimental measurements are consistent with the $\mathbf{k}_n$ version (thus bearing out Durand's conjecture), and completely inconsistent with the $(\mathbf{p}^*-\frac{1}{2}\mathbf{q}^*)$ version. This will be discussed later where the experimental comparison is made. From now on the $\mathbf{k}_n$ version will be used unless specifically stated to the contrary.

The fundamental consideration, of course, is the size of each of the various terms. This is best shown in graphic form, depicting the triply differential cross section as a function of ω^* for various values of the electron scattered energy E'. Figure 4 shows $q^2=10$ F^{-2} at $\theta=20°$, for E' at the top of the quasi-elastic electron peak. Also shown in Fig. 4 are the values of ω(lab) which correspond to the ω^* values. *The e-p coincidence detectors in this experiment subtended only the forward cone*, that is only angles in ω(lab) less than about 20° (for $q^2=10$ F^{-2}).

The counters were designed to include more than 99% of the protons from the big S-state proton term, for electrons at the top of the quasi-elastic peak. Notice, however, that many of the other terms contribute a significant fraction of their cross section in the region of ω greater than 20° (lab). Thus, these terms dominantly affect the number of events in the (e, not p) category, that is, the events which would otherwise be assigned to e-neutron scattering. The exceptions to this are the S-D n-p interference term and the double derivative proton term. The first is negative, the second positive. Both contribute to reducing or increasing the number of particles in the $(e+p)$ coincidence category, especially in the tails of the momentum spectrum of the scattered electron.

The D-state term is the most model-dependent term. Its absolute magnitude in the region of the peak is roughly proportional to the D-state probability, which is not yet a well-known quantity from low-energy experimental data. Various D-state probabilities (3%, 5%, or 7%, say) have a substantial systematic effect upon the fractional acceptance of the D-state protons within our counter solid angle.

Figure 5 shows the electron-momentum spectrum at $q^2=10$ F^{-2}, with all of the various terms drawn in. The net effect of each of the various terms is summarized in Table II for both the $q^2=10$ F^{-2} point and the $q^2=70$ F^{-2} point. All calculations assume a modified Hulthèn model with a 5% D-state probability.

C. Comparisons among Wave-Function Models

There are two dominant parameters which characterize the deuteron wave-function models used in the present analysis: first, the D-state probability; and second, the presence or absence of a "hard-core" radius, within which the wave function is set equal to zero. There are many models for the wave function. The model used in

TABLE II. Sizes of various theoretical terms at $q^2=10$ and 70 F^{-2}.[a]

Term	Relative size of $d^2\sigma/d\Omega dE'$ at E'_{peak} $q^2=10$	$q^2=70$	Relative size of $\int dE'(d^2\sigma/d\Omega dE')$ $q^2=10$	$q^2=70$
S-state protons	1	1	0.961	0.965
neutrons	0.28	0.39	0.265	0.376
n-p interference	0.00004	0.000003	0.001	0.0001
D-state protons	0.011	0.012	0.050	0.050
neutrons	0.0030	0.0045	0.014	0.020
n-p interference	0.00002	7×10^{-7}	0.001	2×10^{-5}
$S-D$, n-p interference	−0.004	−0.001	−0.007	−0.002
Doubly derivative protons	0.0025	0.0028	0.005	0.005
neutrons	2×10^{-5}	...	10^{-5}	...
n-p interf.	2×10^{-5}	...	10^{-5}	...
Convection current protons	0.0016	0.0008	0.0026	0.0013
neutrons	2×10^{-5}	...	0.0003	...
n-p interf.	2×10^{-5}	...	3×10^{-6}	...

[a] *Note.* At $q^2=70$, the blank entries show those terms which are proportional to the neutron form factor F_{1n}, whose value is unknown.

almost all of the analysis described in this paper is the "modified Hulthèn" model.[25] It has the enormous calculational advantage of being analytic:

$$u(R)=N\ (\cos\epsilon)[e^{-\alpha R}-e^{-\beta R}][1-e^{-\beta R}], \quad (12.1)$$

$$w(R)=N(\sin\epsilon)[e^{-\alpha R}][k^2][1+3k/(\alpha R) +3k^2/(\alpha^2R^2)], \quad (12.2)$$

where k is given by

$$k=(1-e^{-\mu'\alpha R}). \quad (12.3)$$

The constant α is determined by the binding energy, and $e^{-\alpha R}$ dominates the asymptotic behavior; N is determined by α and the effective range; and $(\tan\epsilon)$ is determined largely by the deuteron quadrupole moment.

The value of β is determined by the normalization requirement on $u(R)$, and is a function of the S-state probability. Similarly, the value of μ' is determined by the D-state probability through the normalization condition on $w(R)$. The values chosen for the various parameters in the modified Hulthèn wave function are listed in Table III for various D-state probabilities and various effective ranges.

Two other deuteron models were also used in data analysis: the Hamada-Johnston wave function[26] and a wave function developed by Feshbach and Lomon.[12] Both are presented in tabular form rather than as analytical functions of R. The low-energy parameters which they fit are also shown in the table. Both of these models are characterized by a "hard-core" radius.

Note that both the Hamada-Johnston model and the Lomon-Feshbach model fit slightly different low-energy parameters. For a direct comparison with the modified Hulthèn model it is necessary to generate a modified Hulthèn wave function which fits the *same* low-energy parameters. The two corresponding modified Hulthèn wave functions are also shown in Table III.

[25] L. Hulthén and M. Sugawara, *Handbook of Physics* (Springer-Verlag, Berlin, 1957), Vol. 39.

[26] T. Hamada and I. Johnston, Nucl. Phys. 34, 382 (1962).

The wave function enters into the results reported here in two important ways: First, it affects the shape of the proton recoil spectrum and the correction due to the number of protons thrown outside of our counter acceptance; and second, it affects the shape of the electron scattered-momentum spectrum, and the correction due to the number of electrons outside our momentum bite. The first item dominantly affects the σ_n/σ_p ratio

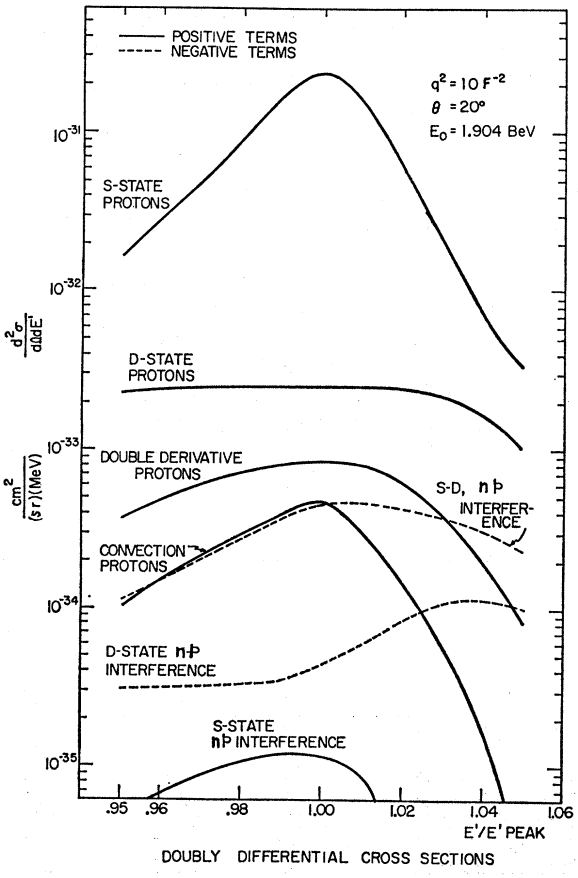

FIG. 5. Doubly differential cross sections at $q^2=10\ F^{-2}$, $\theta=20°$.

TABLE III. Wave-function models and low-energy parameters.

Name of model	Probabilities P_D	Probabilities P_S	N^2 (F^{-1})	α (F^{-1})	β (F^{-1})	μ'	$\sin(\epsilon)$	Effective range $\rho(-\epsilon_t, -\epsilon)$ (F)
Modified Hulthén	0.03	0.97	0.7769	0.2317	1.7433	2.76	0.02750	1.742
Modified Hulthén	0.05	0.95	0.7769	0.2317	1.6790	3.28	0.02750	1.742
Modified Hulthén	0.07	0.93	0.7769	0.2317	1.6182	3.65	0.02750	1.742
Hamada-Johnston	0.07	0.93	0.78555	0.2317	...	...	0.02556	1.770
Modified Hulthén	0.07	0.93	0.78555	0.2317	1.5883	3.83	0.02556	1.770
Lomon-Feshbach	0.055	0.945	0.78402	0.2317	...	...	0.02770	1.765
Modified Hulthén	0.055	0.945	0.78402	0.2317	1.6370	3.35	0.02770	1.765

data, while the second is a correction to the hydrogen/deuterium ratio data.

We will compare the three modified Hulthèn models given in Table III with D-state probabilities of 3%, 5%, and 7%. Table IV shows the missing-proton fractions for the $q^2=20$ F^{-2} case, for electrons at the top of the quasi-elastic peak. Note that the fraction (of missed S-state protons) is very small for a counter subtending 15.5° (polar angle) in the laboratory, and is also very insensitive to the D-state probability. The fraction of missed D-state protons is large, ranging from 20 to 37%, which leads to a strong dependence on *the D-state probability*. The total amount missed is seen to be 0.36, 0.46, and 0.60% for D-state probabilities of 3, 5, and 7%. *This is a source of systematic error* in the σ_n/σ_p ratio measurements; its effect on that ratio is magnified by factors of from two to four.

The effect on the electron momentum spectrum is also large. This is shown in Table V for the $q^2=10$ F^{-2} case. Note that the missing electrons (for a momentum cutoff 5% below the peak) comprise 6.35, 7.15, and 7.95% of the total for D-state probabilities of 3, 5, and 7%. This is also a *source of systematic error* in the hydrogen/deuterium ratio measurements.

The variation in the experimental correction factors because of differences among the several wave-function models is smaller than the variation due to the uncertainty in the D-state probability. We consider two comparisons: that between the Hamada-Johnson (7%) model and the modified Hulthèn model which fits the same low-energy parameters; and that between the Lomon-Feshbach model and its corresponding modified Hulthèn (5.5%) model.

Table IV shows the effect on the number of missed protons at $q^2=20$ F^{-2}. Note that the differences are less than 0.05% which is far smaller than the variation due to a change in the assumed D-state probability. Note also that the amount missed is very close to the value predicted from the modified Hulthèn models which were used in the analysis and which fit better low-energy parameters. In other words, slight changes in the low-energy parameters have very little effect upon our final conclusions.

The fraction of electrons missed because of a momentum cutoff 5% below the peak is shown in Table V. Note here also that there are only very small differences among the various models, except as given by the differences in the D-state probability.

No theoretical studies have been made within the scope of this paper attempting to compare the effect of various model assumptions upon the "small" terms, such as the n-p interference and the convection current terms. It is assumed that the variations are only a small fraction of the size of each of these terms, although it is obvious that the D-state probability will act as a scaling factor on the sizes of the D-state terms.

It is also important to note that there is negligible variation with q^2 in the differences among the various models; this was checked by a study of the theoretical cross sections at $q^2=70$ F^{-2} as well as at $q^2=10$ F^{-2}.

TABLE IV. Missed protons at top of quasi-elastic peak for various models ($q^2=20$ F^{-2}).

Model	Probabilities P_S	Probabilities P_D	D/S ratio of proton big terms at top of quasi-el. peak (%)	Fraction of protons from this state outside of 15.5° (lab) S-state F_S (%)	Fraction of protons from this state outside of 15.5° (lab) D-state F_D (%)	Fraction of all protons missed $=F_SP_S$ or F_DP_D F_SP_S (%)	Fraction of all protons missed $=F_SP_S$ or F_DP_D F_DP_D (%)	Total fraction of protons missed (%)
Modified Hulthén	0.97	0.03	0.80	0.21	20	0.20	0.16	0.36
Modified Hulthén	0.95	0.05	1.11	0.16	28	0.15	0.31	0.46
Modified Hulthén	0.93	0.07	1.34	0.12	37	0.11	0.49	0.60
Hamada-Johnston	0.93	0.07	1.33	0.14	36.5	0.13	0.48	0.61
Modified Hulthén	0.93	0.07	1.34	0.12	36.0	0.11	0.49	0.60
Lomon-Feshbach	0.945	0.055	1.20	0.19	32	0.18	0.38	0.56
Modified Hulthén	0.945	0.055	1.20	0.17	30	0.16	0.36	0.52

TABLE V. Electrons missed below E' cutoff at $(0.95)E'_{\text{peak}}$ for $q^2=10$ F^{-2}.

Model	Probabilities P_S	Probabilities P_D	S state % detected	S state % missed	D state % detected	D state % missed	Total % missed
Modified Hulthén	0.97	0.03	92.6	4.4	1.05	1.95	6.35
Modified Hulthén	0.95	0.05	91.1	3.9	1.75	3.25	7.15
Modified Hulthén	0.93	0.07	89.6	3.4	2.45	4.55	7.95
Hamada-Johnston	0.93	0.07	89.5	3.5	2.45	4.55	8.05
Modified Hulthén	0.93	0.07	89.6	3.4	2.45	4.55	7.95
Lomon-Feshbach	0.945	0.055	90.4	4.1	1.95	3.55	7.65
Modified Hulthén	0.945	0.055	90.7	3.8	1.95	3.55	7.35

IV. EXPERIMENTAL METHOD

Electrons from the external beam of the Cambridge Electron Accelerator struck a liquid-hydrogen or deuterium target. The scattered electrons were detected in a magnetic spectrometer followed by a Čerenkov and a shower counter. The momentum acceptance of 15% was divided into 1% bins: the momentum resolution was approximately 2.5% (full width at half-maximum). Protons were detected in a two-counter telescope of large solid angle, protected from the high background fluxes of low-energy particles either by lead absorber or by a sweeping magnet. A 12×12 checkerboard counter hodoscope was used to measure the angular distribution of recoiling protons. The layout of the apparatus is shown schematically in Fig. 1.

The discriminated outputs of all counters and pulse height information from the shower, Čerenkov, and proton counters were connected through an interface to an on-line PDP-1 computer. The correlated counter information for each event, together with other parameters relevant to the running of the experiment was stored on magnetic tape for subsequent event-by-event reanalysis. The basic event trigger for the computer was generated by the detection of a charged particle crossing the focal plane of the electron spectrometer with an associated shower-counter pulse height larger than some small predetermined bias level; the Čerenkov counter was not included in the trigger logic. The criterion for generating a trigger was deliberately kept very nonselective in order to minimize the possibility of missing genuine events.

The apparatus will be described in more detail in a forthcoming paper on elastic electron-proton scattering.

V. METHOD OF DATA ANALYSIS

There were two steps in the analysis of the raw data:

(i) A study of the shower and Čerenkov spectra in order to decide on bias levels sufficiently high to ensure that all events accepted were genuine electrons; also, a study of the possible contamination above the chosen bias level by examination of the spectra of rejected events.

(ii) A study of the nature of the electron trajectory information in the momentum counters, sorting events into "perfect" and "nonperfect" categories; then, the establishment of criteria for accepting and rejecting events on the basis of the information in the momentum-counter array.

A. Shower- and Čerenkov-Counter Spectra

The basic electron identification is through the presence of a large pulse in both the shower- and the Čerenkov-counter spectra.

Typical scatter-plots showing the correlation between the shower and the Čerenkov pulse heights are shown in Fig. 6. In these scatter plots, deuterium events in the (e, not p) category are shown. The most important aspects are that at the low q^2, the Čerenkov counter alone provides almost all of the rejection, while at the higher q^2 the shower counter is most important but still not entirely self-sufficient.

The fraction of all computer triggers which ended up being rejected *solely* on the basis of the shower and Čerenkov criteria represents an increasing fraction of the total as q^2 increases. Only 3.2% of all computer triggers are rejected at $q^2=7$ F^{-2}, while at $q^2=70$ F^{-2} the fraction is 68%, with only 32% surviving. It is important to note, however, that these numbers are sensitive to the exact value of the (fairly low) shower-counter discrimination level in our fast electronic trigger logic.

Bias levels were chosen conservatively, typically introducing from 2% to 8% inefficiency in each counter. The absolute efficiency of the shower counter for the bias chosen was measured by examining the shower spectrum for perfect-trajectory events with a high Čerenkov pulse height required, and the Čerenkov efficiency was determined in the opposite way, requiring a high shower pulse.

The crucial consideration is an estimate of how many events other than genuine electrons could possibly have been accepted by our criteria. The estimate will be given in detail for the $q^2=30$ F^{-2} point.

Figure 7 shows the spectrum of the shower counter for all perfect-trajectory events with pulse height below channel 5 in the Čerenkov counter, and also the Čerenkov spectrum for all perfect-trajectory events below channel 18 in the shower counter. The full spectra for both counters are also shown, as well as the bias levels chosen for eventual analysis of the data. From these

data, the low-shower events have a 2.5% chance of having a Čerenkov pulse greater than the chosen bias, while the low-Čerenkov-pulse events have a 2.4% chance of having a shower pulse greater than the bias. *Assuming no correlation*, the net probability is the product of the two individual probabilities, or 0.06%. Since the total number of rejected events is 30% of the total of accepted events, only about 0.02% of the events in our accepted region could have crept in from the low-pulse-height region because of a double, uncorrelated high-Čerenkov and high-shower occurrence. The assumption that the rejected events exhibit no correlation between shower and Čerenkov pulse heights is not necessarily correct.

However, the only process which seems to have a possibility of yielding a correlation is the charge exchange of a negative pion

$$\pi^-+Z\rightarrow\pi^0+Z'$$
$$\searrow$$
$$\gamma+\gamma$$
$$\searrow e^++e^-.$$

If this were to occur within our counter array, a subsequent count by the electron-positron pair in both the Čerenkov and shower counters could simulate a genuine event. The above process is calculated to occur 0.08% of the time. It thus introduces negligible contamination in our data.

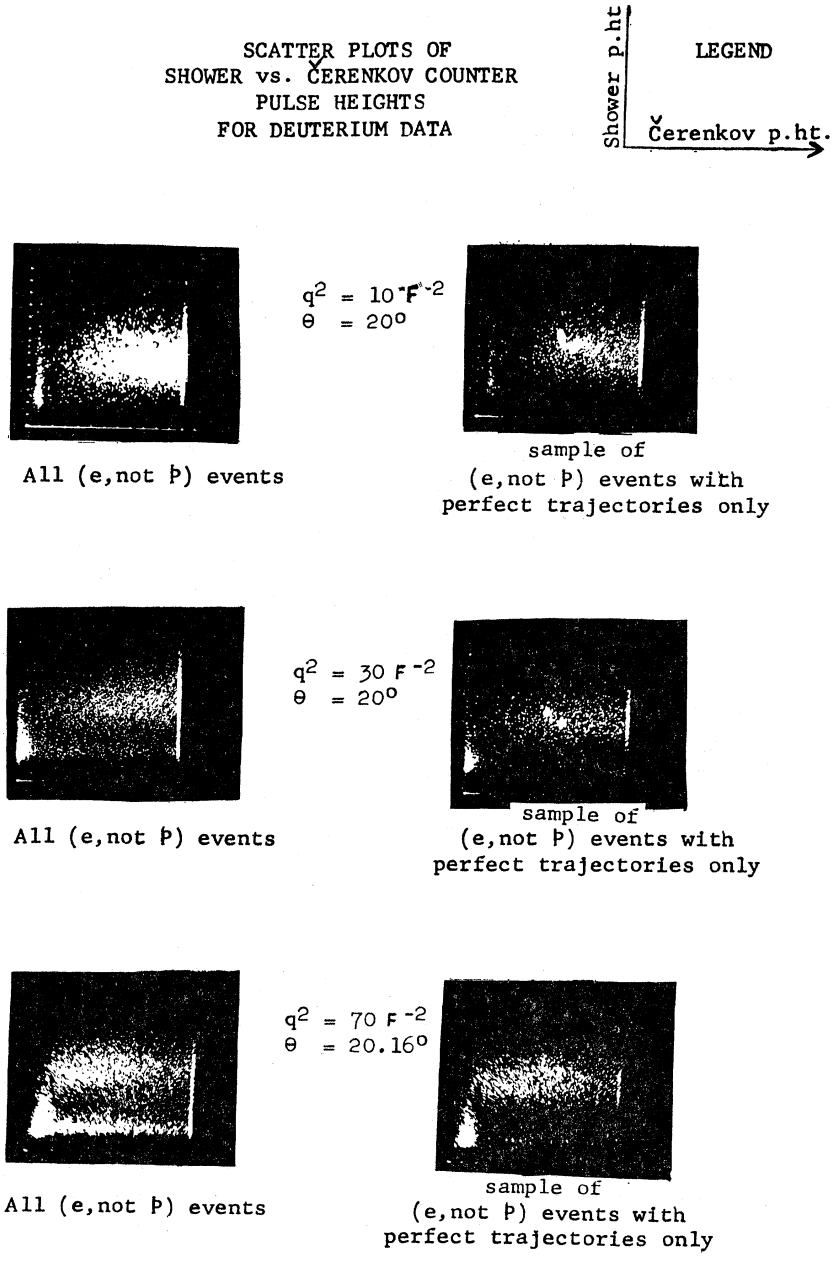

FIG. 6. Scatter plots of shower versus Čerenkov-counter pulse heights for deuterium (e, not p) data.

Electrons from background processes other than those already considered can enter our spectrometer system and contaminate our sample of elastic and quasi-elastic events. In fact, it is even possible that such electrons might be associated with correlated coincidence protons, thus appearing to be elastic or quasi-elastic electron-proton coincidence events.

One possible process is electroproduction of π^0, with a Dalitz-decay electron passing into our spectrometer acceptance:

$$e+p \rightarrow e+p+\pi^0$$
$$\searrow$$
$$\gamma+e^+ + e^-.$$

An approximate calculation of the magnitude of this effect indicates that the contamination from this process and others like it is completely negligible at the low-q^2 points, but is an increasingly more significant effect as q^2 increases. At $q^2=7$, 70, and 115 F^{-2}, the fractional effect compared with elastic e-p scattering is calculated to be (2×10^{-7}), (2×10^{-4}), and (5×10^{-3}). Several other possible processes are not included in the calculation, the most important omissions being the multiple-pion production and peripheral processes.

B. Momentum Definition

An event surviving the shower- and Čerenkov-counter biases was then placed in a given momentum interval by using the pattern of struck counters in the electron spectrometer to determine where the electron crossed the focal plane. Typical "perfect trajectory" events are shown schematically in Fig. 8.

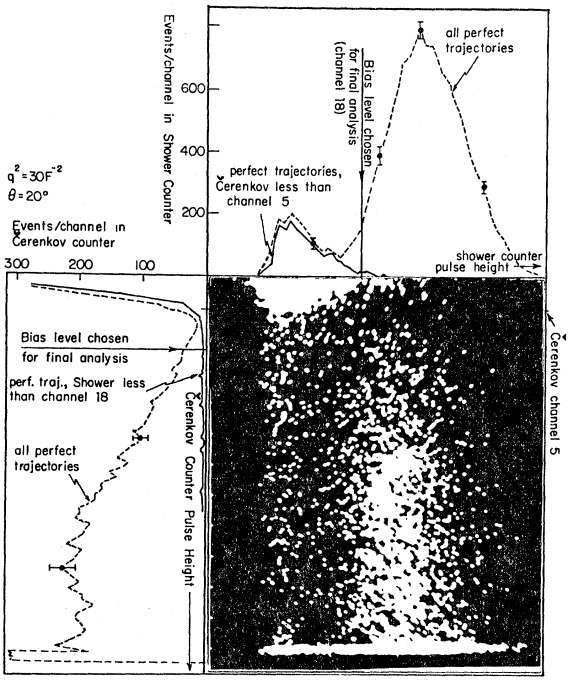

FIG. 7. Shower versus Čerenkov scatter plot, $q^2=30$ F^{-2}.

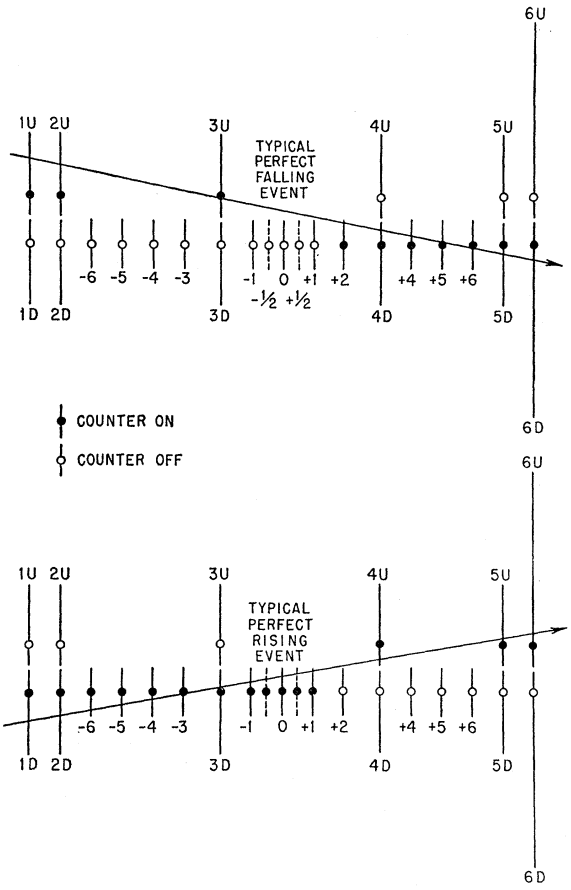

FIG. 8. Typical perfect trajectories in counter array.

The σ_n/σ_p ratio data reported in this work use only those electrons with either a perfect trajectory or only one imperfection; such as a single additional counter or a random coincidence. However, since these events comprised approximately 98% of all acceptable events, the inclusion of the other events would have negligible effect on the final results.

C. Electron-Proton Coincidence Information

Having determined which events among all of the triggers were "good electrons," the next step was to decide whether or not a coincident proton signature was present. This was done using the coincidence bit $(e+p)$ representing the result of a fast coincidence taken between electron and proton counters, which was sent to the computer for storage with each event. The entire ensemble of events was broken down into two groups: those with the above bit present and those without it. It was important to check that the two ensembles of eventually-accepted events had identical signatures within the electron-arm data (identical shower and Čerenkov spectra; and identical distributions among the various categories in the trajectory-defining system). Except for statistical fluctuations, this was found to be true for each datum point.

TABLE VI. Chance probabilities in proton-detecting telescope.

q^2 (F^{-2})	θ	Final H_2 chance rate (%)	Final D_2 chance rate (%)	Correction factor due to spill structure (%)
7	20°	1.64±0.12	1.76±0.10	8
10	20°	2.13±0.12	1.83±0.08	9
15	20°	2.62±0.18	1.76±0.08	11
20	20°	3.4 ±0.3	3.2 ±0.2	8
30	20°	4.8 ±0.6	7.2 ±0.4	15
45	20°	5.2 ±0.3	6.0 ±0.2	12
70	20.16°	6.6 ±0.6	4.7 ±0.3	9
115	29.64°	···	6.9 ±0.5	11
15	90°	···	4.6 ±1.4	9

The method used to set the high voltages and discrimination levels on the proton counters employed a calibration using elastic scattering from hydrogen, with its well-defined kinematics. The following ratio was then examined: $(e+p)/(\text{all } e)$. This ratio, called the "e-p efficiency," was typically between 95% and 97%. Target-wall electron scattering and proton absorption account for essentially all the remaining 3% to 5% "inefficiency."

At a beam intensity sufficiently low that rate-dependent effects were not a problem, the high voltage on each individual counter was adjusted until the apparent proton efficiency remained constant with the input pulses to the discriminators attenuated by: +4 dB, +2 dB, and 0 dB, with 0 dB being the normal operating condition. The photomultiplier gains were estimated to be stable to within approximately ±2 dB; 4 dB was used as an additional safeguard against efficiency changes.

D. Rate-Dependent Checks

Once the counter high voltages had been set, rate-dependent studies were made. With the discriminators set at the 0 dB position, the beam intensity was gradually raised and the apparent efficiency was monitored. Eventually, at instantaneous singles counting rates of about 10–15 MHz the efficiency began to decrease. Recent tests[27] show that dead time in the Chronetics-101 discriminators and rate-dependent effects in the 102 coincidence units were probably to blame.

If the beam intensity at which the falloff in efficiency was barely significant (about 1%) is termed I_f, then the method used was to take the actual data at intensities of less than or equal to $(0.5)I_f$. Both hydrogen and deuterium data were taken at identical "effective intensities," as measured by the criterion of identical double-coincidence chance probabilities in the electronic circuitry. Compared with the hydrogen running, the actual beam intensity had to be dropped by about 30% in the deuterium running to equalize the "effective intensity."

One of the problems with the experiment was the difficulty in gaining confidence in the rate-dependent studies. At the higher q^2 points, the hydrogen elastic counting rates were too low to permit rate studies to be performed in the data-taking conditions. In these cases, it was necessary to change the kinematic conditions to a lower q^2 and then to perform the calibrations and rate studies in the high-rate, low-q^2 situation. Since low-energy protons ionize more highly than higher-energy ones, a few dB of additional attenuation were added to the raw pulses before discrimination to reduce the pulses to the same height as the real higher-energy pulses which would occur in the actual high-q^2 data taking.

E. Chance-Rate Corrections

The chance coincidences were monitored by a delayed-coincidence technique in which the proton counter signal was effectively delayed by 35 nsec relative to the electron-proton coincidence timing. This time separation was sufficiently long that no overlap of genuine coincidences was possible. A correction to this measured chance probability of about 10% was necessary because of the structure of the beam "spill." The chance rates, the corrections, and the errors are listed in Table VI for the various data points.

F. Proton-Counter Solid Angles

It is important to tabulate the solid angles subtended by our proton-detecting counters, because theoretical corrections due to losses of protons thrown outside of our detection system are sensitive to the subtended solid angle.

The "effective" solid angle is arrived at by folding in several effects: the counter shapes and sizes and their locations; the effect of the finite electron aperture; the target length effect; and the multiple Coulomb scattering in the lead absorber where applicable. There is also another effect: the change in the direction of the momentum-transfer vector ($\mathbf{q}_v$) as E' varies across the quasi-elastic electron peak. Because of this change, the fraction of the proton cone subtended by the counters depends on E'.

With the presence of aperture, target-length, multiple-scattering, ($\mathbf{q}_v$) change, and counter shape effects, it is difficult to quote the exact shape of the solid angle. What was done in the data analysis was to integrate over the various effects, using as the proton distribution the S-state angular spectrum. We then define the angle ω_c, which is the *effective* acceptance angle, defined as the half-angle of a cone which would have accepted the same fraction of protons. Because of the conical symmetry of the theoretical cross section, this approximation greatly simplifies the calculation of the theoretical corrections due to other (small) cross section terms. In two specific cases, detailed checks showed that the approximation led to no significant errors in the theoretical corrections.

[27] T. M. Knasel (private communication).

TABLE VII. Proton counter solid angles in laboratory. (Tabulation shows ω_c, half-angle of "effective" cone.)

E'/E'_{peak} \ q^2 (F^{-2}), θ	7, 20°	10, 20°	15, 20°	20, 20°	30, 20°	45, 20°	70, 20.16°	115, 29.64°	15, 90°
0.94	20.8°	15.9°	13.9°	...	9.5°	...	...	...	15.0°
0.95	21.8°	16.9°	15.0°	11.6°	10.5°	10.0°	7.2°	...	...
0.96	22.9°	18.1°	16.2°	12.7°	11.4°	10.9°	7.7°	...	15.1°
0.97	23.9°	19.0°	17.4°	13.7°	12.3°	11.3°	8.2°	...	...
0.98	24.7°	19.7°	18.8°	14.3°	12.9°	11.8°	8.2°	...	15.3°
0.99	25.3°	20.4°	18.8°	14.9°	13.8°	11.9°	8.3°	...	...
1.00	26.1°	20.7°	18.9°	15.1°	14.0°	12.0°	8.4°	5.35°	15.5°
1.01	25.3°	20.4°	18.8°	15.0°	13.9°	11.9°	8.3°	...	...
1.02	24.7°	19.7°	18.8°	14.4°	13.4°	11.7°	8.3°	...	15.3°
1.03	23.8°	19.0°	17.3°	13.7°	12.7°	11.2°	8.2°	...	...
1.04	22.8°	17.9°	16.0°	12.5°	11.9°	10.5°	7.7°	...	15.1°
1.05	...	16.8°	15.4°	11.4°	10.9°	9.6°	7.1°	...	...
1.06	...	...	13.5°	9.8°	9.7°	...	6.6°	...	15.0°

Table VII contains a tabulation of the half-angles ω_c. The values are tabulated for various E' points across the quasi-elastic peaks.

VI. ABSORPTION AND CONVERSION CORRECTIONS

A proton emerging from the target has a small probability of not counting in our proton-detecting counter array. The causes of this are three in number:

(a) large-angle proton scattering in the target;
(b) proton absorption or scattering within the air and lead located between the target and the counters;
(c) proton absorption within the scintillators themselves.

Conversely, a neutron emerging from the target does have a small probability of producing a count in our counters. Three reasons for this, closely related to the reasons for proton absorption just listed above, are

(a) neutron-proton charge-exchange scattering within the target, with a high-energy proton emerging;
(b) neutron conversion within the air path and lead;
(c) neutron conversion within the scintillators themselves.

The corrections due to all of these effects are dealt with by making either experimental or calculational estimates (or both) of the sizes of the effects. The ratio [$(e+p$ coincidences)/(all electrons)], measured in the hydrogen data, is taken as a measure of the proton absorption effects. The correction can be calculated from available data, and the results compared. The neutron conversion correction had to be determined solely by calculation, because it was not possible to measure it in this experiment.

The nucleon-nucleon cross sections were taken from the compilation by Wilson.[21] The cross sections were taken from the papers of Chen,[28] Batty,[29] and Williams.[30] Using these, the absorption probability of protons within lead and scintillator is calculated to be 0.032 and 0.009 per linear centimeter traversed, respectively.

The neutron conversion probability must be calculated from data similar to that used in calculating the proton-absorption probability. An indication of the reliability of the calculation is probably given by the comparison between experiment and calculation for the proton absorption case. A comparison shows that at low q^2 there is excellent agreement, within 10%. At the higher q^2, the calculation is probably not reliable to better than 30%.

The pertinent neutron cross sections are the total inelastic cross sections taken from the papers of Harding,[31] Millburn,[32] Batty,[29] Chen,[28] and Coor.[33] The errors in the calculation are dominated by uncertainties in the effective thickness for conversion within the scintillators. The effect of the hydrogen within the scintillators is included using $n-p$ charge-exchange cross sections.[21]

The corrections amount to about 0.20% in the cases where no lead absorber was used, and range from about 0.7% to 1.2% where lead was used. The uncertainties in the over-all calculation can best be judged from the fact that the proton absorption calculation agreed with the experimental data only to about $\pm 30\%$ at the q^2 points above 20 F^{-2}. This $\pm 30\%$ error has been assigned to the calculated neutron-conversion corrections.

A comparison between the calculated and experimentally determined values for the proton absorption probability is shown in Fig. 9. It can be seen that there is excellent agreement between calculation and experiment at $q^2=7$, 10, and 15 F^{-2} which are the points in which the lead absorber was used. The agreement is poorer at the higher q^2 points. The procedure used was to apply the *experimental* corrections to the deuterium data, with their experimental errors.

The proton-absorption corrections measured in the

[28] F. F. Chen, C. P. Leavitt, and A. M. Shapiro, Phys. Rev. **99**, 857 (1955).
[29] C. J. Batty, Nucl. Phys. **23**, 562 (1961).
[30] R. W. Williams, Rev. Mod. Phys. **36**, 815 (1964).
[31] R. S. Harding, Rochester Report No. NYO-8056, 1958 (unpublished).
[32] G. Milburn, W. Birnbaum, W. Crandall, and L. Schecter, Phys. Rev. **95**, 1268 (1954).
[33] T. Coor, D. Hill, W. Hornyak, L. Smith, and G. Snow, Phys. Rev. **98**, 1369 (1955).

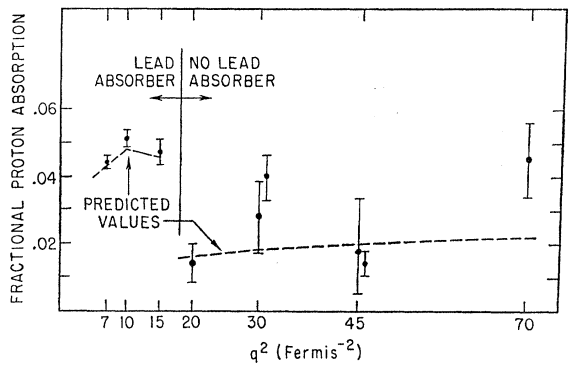

FIG. 9. Comparison between theory and experiment for proton absorption.

hydrogen data cannot necessarily be carried over directly to the deuterium data, because the angular distributions of protons are different in the two cases. The protons from hydrogen all strike near the center of the counters, while the protons from deuterium are spread out over more of the total counter areas. The only major effect is the variation in proton recoil energy as a function of the electron scattered energy E'. The protons are less energetic for electrons near the deuteron-breakup threshold and more energetic on the other side of the quasi-elastic peak. However, the absorption cross sections are such slowly varying functions of proton energy that this is a negligible effect except at $q^2=7$ F^{-2}. Here, the extra absorption (and, in fact, the range limitation for the very lowest-energy protons) results in an additional calculated correction amounting to 0.65% of all protons. The same correction is estimated to be less than 0.05% at $q^2=10$ F^{-2}.

VII. RADIATIVE CORRECTIONS

A. Elastic *e-p* Radiative Corrections

The basic radiative correction for elastic $e-p$ scattering is taken from Eq. (4.1) of Meister and Yennie.[34] If the measured cross section is σ_M, then the hypothetical cross section which would have been measured in the absence of radiation is given by σ_R:

$$\sigma_R=\sigma_M e^{-\delta}=\sigma_M e^{(-\delta_{\rm I}-\delta_{\rm II}-\delta_{\rm III})},$$

where the correction factor δ has broken up into the sum of three terms. $\delta_{\rm I}$ is a refined expression for the well-known Schwinger correction for radiation by the electron line. Meister and Yennie can justify exponentiation of this part of the correction, in order to take account of the higher-order terms in the fine-structure constant. $\delta_{\rm II}$ contains the contribution due to the interference between electron-line and proton-line radiation, while $\delta_{\rm III}$ contains several other small terms in the square of the proton-line radiation diagrams. Although exponentiation of the $\delta_{\rm II}$ and $\delta_{\rm III}$ terms cannot be rigorously justified, it was performed in this analysis in the hopes of obtaining a better approximation for the over-all correction. The effect of exponentiation is very small in all cases. We have included a correction to the Meister and Yennie calculation which attempts to take account of the variation of the basic cross section in the case of radiation before scattering. This is discussed in the next section.

B. Electron-Deuteron Radiative Corrections: Meister and Griffy

The quasi-elastic deuteron peak has a finite width and thus must be expressed as a doubly-differential cross section: $d^2\sigma/d\Omega dE'$. This fact complicates the calculation of the radiative correction to the quasi-elastic scattering process. For scattered electrons with energies (E') far below the region of the main quasi-elastic peak, the width of the peak should not matter: The radiative correction should approach that which would be calculated for an elastic δ function at the peak position. The complication only arises when one needs to calculate the correction in the region of the main peak itself when the peak shape becomes an important parameter in the radiative correction calculation. It was originally intended that the work of Meister and Griffy[35] would be used to apply the radiative corrections to the quasi-elastic peak. However, because of uncertainties in the method for applying Meister and Griffy's recipe, another technique, the "δ-function" method, was used.

We discuss the uncertainties in Meister and Griffy's recipe because most previous noncoincidence data analysis has employed it.[13,14,16] The way in which we attempted to apply Meister and Griffy's calculation to quasi-elastic electron-deuteron scattering has been discussed in detail by Dunning.[16] The calculational method employed by Meister and Griffy for the electron-line radiation is to split the radiative correction up into "hard" and "soft" contributions. A cutoff energy δE is introduced. Any radiation of photons with energy below δE is said to be "soft": it is assumed that it is not necessary to take into account the variation of the cross section in the calculation of this part of the correction.

Radiation of photons with energy above δE is assumed to be "hard": Here, the calculation takes into account the fact that the cross section varies as a function of q^2 and E'. The "peaking approximation" is then used: The "hard" radiation is assumed to occur only along the directions of the incident and final electron lines. The trick is to discover a broad region over which δE can be varied without affecting the *sum* of the hard and soft corrections.

When the calculation was performed by computer, the sum ($\delta_{\rm soft}+\delta_{\rm hard}$) showed strange behavior. Figure 10 shows that at any given E' the sum ($\delta_{\rm soft}+\delta_{\rm hard}$) goes through two "stable regions," one in the 10–100

[34] N. Meister and D. Yennie, Phys. Rev. **130**, 1210 (1963).

[35] N. Meister and T. Griffy, Phys. Rev. **133**, B1032 (1964).

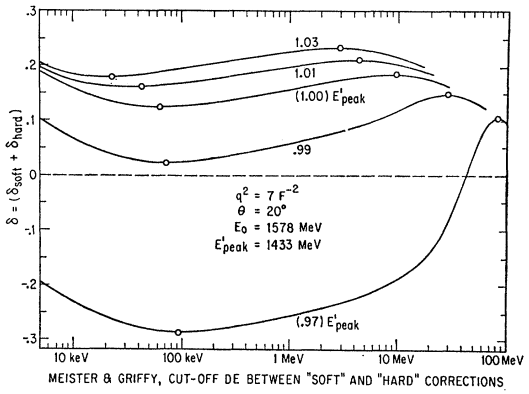

FIG. 10. Meister and Griffy radiative-correction calculation: $(\delta_{\text{soft}}+\delta_{\text{hard}})$ as a function of cutoff.

keV region and the other in the 5–100 MeV region. In Meister and Griffy's article, the examples given in their table choose the higher stability point. In our $q^2=7$ F^{-2} case, this occurs at $\delta E=10$ MeV for $E'=E'_{\text{peak}}$.

Meister and Griffy then assume that the radiative correction for E' values away from the peak is arrived at by using the value of $(\delta_{\text{soft}}+\delta_{\text{hard}})$ for the same (10 MeV) value of δE. However, the prescription is invalid away from the peak. First, 10 MeV no longer corresponds to a "stability point" in the sum $(\delta_{\text{soft}}+\delta_{\text{hard}})$. Second, if one allows this "stability point" to vary with E' in order to achieve a flat region for each value of E' separately, then one is forced to consider very large values of δE for E' below the top of the peak. These large values (100–200 MeV, and even larger) correspond to almost no "hard" radiation at all, and are physically untenable.

The existence of another region of stability (10–100 keV in our particular case) was probably not known to Meister and Griffy, nor to other authors (Hughes *et al.*[13]; Dunning *et al.*[16])who used Meister and Griffy's work. The latter two experimenters employed the higher cutoffs in their deuteron radiative corrections. Using the lower cutoff values (in the 10- to 100-keV region) seems much more reasonable. However, the uncertainty about exactly which cutoffs to use has led us to reject the Meister and Griffy technique altogether. The "δ-function" method to be described next has been preferred because it has some intuitive motivation, and also because using the hydrogen radiative tail to make the deuterium corrections should help to cancel some possible systematic errors in the comparison of deuterium to hydrogen cross sections.

C. δ-Function Technique

The hydrogen radiative corrections of Meister and Yennie[34] are used to generate the size and shape of the radiative tail from the hydrogen elastic peak in the presence of extremely good resolution. This radiative tail shape is then assumed to represent the radiative process for each small region $\Delta E'$ of the quasi-elastic spectrum, which is a continuum. Let us denote the fractional probability for an electron to go from the elastic δ function into a bin of size $\Delta E'$ centered at a location E' in the hydrogen radiative tail by the function $T(E'_{\text{peak}}-E';\Delta E')$. Besides incident energy and scattering angle, which are suppressed here for convenience, T is a function of two variables: the separation in E' from the energy value E'_{peak} which would have been present without radiation; and the size of the bite $\Delta E'$ around E'.

For the quasi-elastic electron spectrum from deuterium, consider a small bite $\Delta E'$ in the scattered-electron energy spectrum, centered on the energy E'. We are interested in the hypothetical cross section amount $\Delta\sigma_{\text{hyp}}(E')$, which would have been measured in that bite in the absence of radiation. What is actually measured in the bite is the observed cross-sectional amount $\Delta\sigma_{\text{obs}}(E')$. The important assumption is made that $\Delta\sigma_{\text{obs}}(E')$ differs from $\Delta\sigma_{\text{hyp}}(E')$ because of two separate and distinct processes: radiation *out* of the $\Delta E'$ bin, and radiation *into* it from above. The two cross sections are then assumed to be related by

$$\Delta\sigma_{\text{obs}}(E')=\Delta\sigma_{\text{hyp}}(E')e^{-\delta_{\text{out}}}+\int^{\infty}\sigma_{\text{hyp}}(E'')T(E''-E';\Delta E')dE''.$$

The number δ_{out} is the radiation out correction. It is only a function of the $\Delta E'$ bite size, and is given directly by Meister and Yennie's formulation. The integral accounts for the radiation into the bin from above. The integration is over all E'' values *greater than the upper edge of the* $\Delta E'$ *bin.* The upper end (∞) of the integral is actually limited by the fact that the cross section $\sigma_{\text{hyp}}(E')$ has a cutoff at the threshold for quasi-elastic scattering.

The calculational technique is to use the theoretical deuteron cross section as the unradiated peak shape $\sigma_{\text{hyp}}(E')$. The folding with the function $T(E''-E';\Delta E')$ is done by computer and is tricky only because T diverges for zero argument. It is thus necessary to cut off the lower bound of the above integral at a value $E'+\frac{1}{2}\Delta E'$ rather than at E'. It is then important to show that the final answer does not depend on the choice of $\Delta E'$, and this was done. In our final calculations, the calculated radiative correction changes by less than 0.1% when the integration-bin size is doubled. In order to achieve this degree of convergence, the integration-bin size had to be decreased to a width of approximately 0.05% of E'_{peak}.

Only the electron-line radiative correction (δ_{I}) of Meister and Griffy is used for the deuterium corrections just described. The other terms (δ_{II} and δ_{III}), corresponding to the proton-line part, are taken into account in a way to be described later. After T is folded with the deuterium peak shape, no further exponentiation is performed.

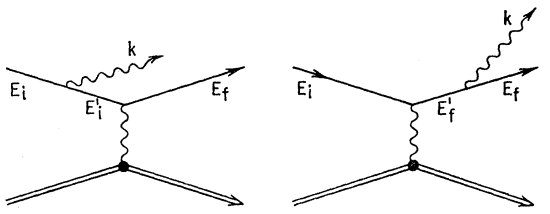

FIG. 11. Feynman diagrams for electron-proton scattering with radiation before and after scattering.

An approximation to the quasi-elastic peak shape is employed for calculational simplicity. The peak shape (for S state only) given in analytic form by Durand[36] is used rather than the full theoretical peak shape of McGee.[3,4] This is estimated to yield a radiative correction differing from the one using the correct theoretical shape by less than 0.2%.

The problem with the variation of the matrix element for radiation before scattering must be discussed. Consider the parts of the radiative correction which Meister and Yennie call the "external parts." For radiation of high-energy photons, two Feynman diagrams dominate, corresponding to radiation before and radiation after scattering. They are shown in Fig. 11.

The calculation of Meister and Yennie makes an approximation by ignoring the fact that the basic electron-nucleon cross section is a function of k, the radiated energy. In the case of radiation after scattering, this approximation is good, but it breaks down for radiation before scattering. The cross section $\sigma(E_i',E_f,\theta)$ is not identical to the unradiated cross section $\sigma(E_i,E_f,\theta)$. Because of the lower "incident" energy, the momentum transfer q^2 is smaller, and the cross section (due to both σ_{Mott} and the form-factor variation) is enhanced. Thus, that part of the Meister and Yennie radiative tail corresponding to radiation before scattering should be increased by a factor of

$$\sigma(E_i',E_f,\theta)/\sigma(E_i,E_f,\theta).$$

Calculations show that almost exactly half of the net final correction δ_I (for large radiative losses) comes from the radiation before scattering. The prescription is therefore to multiply Meister and Yennie's doubly differential cross section in the radiative tail by the factor

$$\tfrac{1}{2}+\frac{1}{2}\left[\frac{\sigma(E_i',E_f,\theta)}{\sigma(E_i,E_f,\theta)}\right].$$

This enhancement is incorporated into the hydrogen radiative tail shape $T(E'_{\text{peak}}-E';\Delta E')$; the new T is then used for the hydrogen and deuterium radiative corrections. Although this approximation may not be precise, the small additional correction almost exactly cancels in the ratio of hydrogen to deuterium cross sections. The peak shapes are affected, as can be seen in

[36] L. Durand, Ref. 2, Eq. (29).

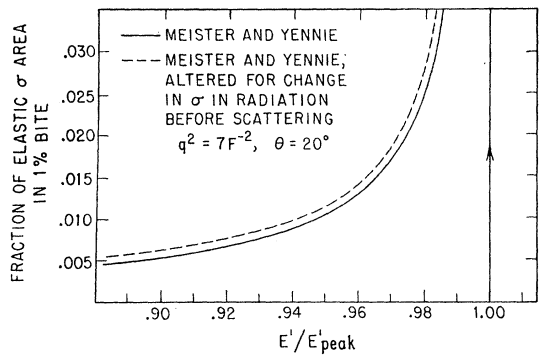

FIG. 12. Hydrogen radiative tails at $q^2=7$ F^{-2}.

Fig. 12. The correction ranges from about 0.5% to about 1.9% in our data.

Figure 13 compares the Meister and Griffy method with the δ-function method for calculating the radiative-correction factor δ. The Meister and Griffy correction is shown using two different prescriptions: a series of different cutoffs in the 10–100-MeV range for various E' values; and a series of different cutoffs in the 10–100-keV range. The δ-function-method results plotted in the figure include the extra correction factor for radiation before scattering.

It should be noted that the δ-function technique and the Meister and Griffy prescription employing the higher cutoffs give corrections identical to within 0.2–0.7% of the cross section at the quasi-elastic peak. The largest differences are at the larger scattering angles. Thus, to this level of accuracy, previous experiments employing the "peak method" of analysis will be unchanged. More substantial corrections apply to data analyzed by the "area method" such as that in Ref. 13.

The radiative-correction calculation described above takes into account electron-line radiation. Any comparison between elastic $e-p$ and quasi-elastic $e-d$ data must take into account the proton-line terms. In order to make a proper comparison between σ_H and σ_D cross

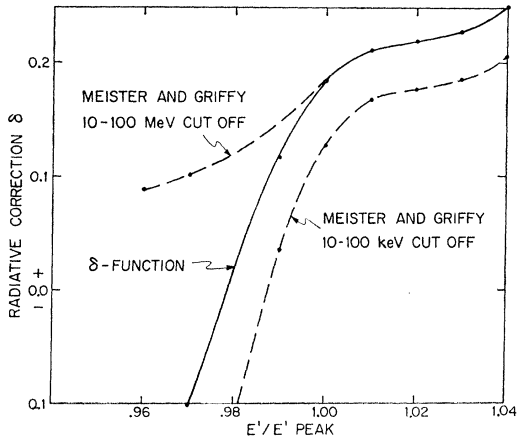

FIG. 13. Various deuterium radiative-correction techniques.

sections, an additional correction was made to the proton part of the deuterium data. What was done was to take the proton-line part of the $e-p$ elastic correction ($\delta_{II}+\delta_{III}$) and to modify the proton part of the quasi-elastic $e-d$ cross section by this additional factor. The *neutron part* was left unaltered, because radiation from the neutron line is entirely negligible.

The fact that a coincidence was used means that a radiative correction should be applied (to both hydrogen and deuterium data) to account for protons missed by our counter telescope due to the altered kinematics in the radiative process, especially in the case of electron radiation of a very hard photon before scattering. However, because this effect is calibrated out in our measurement of the proton detection efficiency for hydrogen, it is largely eliminated as a source of error in affecting either the σ_n/σ_p ratio data or the $(\sigma_{pD}/\sigma_{pH})$ ratio data.

The coincidence radiative correction itself is estimated to be smaller than 0.1% at $q^2=70$ F^{-2}, and to have very little q^2 dependence. No additional correction was applied to any of the data to correct for this effect. The work of Atkinson[37] was used for these estimates.

D. Real Bremsstrahlung

The prescription for losses due to real bremsstrahlung can be found in Heitler[38]:

$$I_{\text{actual}}=I_{\text{observed}}e^{\delta},$$

where

$$\delta=(-1.44t)\ln(\Delta E/E),$$

$t=$ thickness of path in radiation lengths.

For our case, t was equal to about 0.0016 radiation length before scattering, and about 0.0080 radiation length after scattering. The size of the real-bremsstrahlung correction was typically 4%–5%. In the hydrogen/deuterium cross-section ratios reported here, only the *difference* between the corrections for the two cases was applied. This difference was never greater than 0.10%–0.15%, with the deuterium correction being the larger one. The *difference* has been added to the deuterium radiative corrections. The effect of this process upon the σ_n/σ_p ratio data is negligible; no corrections were applied to these ratios.

VIII. ELECTRON-MOMENTUM SPECTRA

After the experimental electron-momentum distributions were generated, certain subtractions and corrections were applied. Among these were the empty-target subtraction, the inelastic (pion-electroproduction) subtraction, and the elastic electron-deuteron scattering subtraction.

[37] R. Atkinson, III (private communication).
[38] W. Heitler, *The Quantum Theory of Radiation* (Oxford University Press, London, 1954), p. 379.

TABLE VIII. Parameters for elastic electron-deuteron scattering.

q^2 (F^{-2})	θ	$\frac{d\sigma}{d\Omega}(ed)\Big/\frac{d\sigma}{d\Omega}(ep)$	$E'(ed)/E'(ep)$
7	20°	0.0132	1.0482
10	20°	0.00523	1.0576
15	20°	0.00194	1.0705

A. Empty-Target Subtraction

Runs with no liquid in the target were taken with each datum point. These runs were analyzed using the same criteria used for the main data analysis. The empty-target events were separated into $(e+p)$ and (e, not p) categories, and were subtracted from the main data within these two categories separately. The size of the empty-target background (within a momentum bite of about 6% around the quasi-elastic peak) ranged from 3% to 5% for our 1-in.-long targets, and from 1.5% to 2.5% for our 2-in.-long cups. About $\frac{1}{3}$ of the empty-target events were typically of the $(e+p)$ coincidence type with the other $\frac{2}{3}$ lacking a coincidence. In the worst case, the additional uncertainty in the σ_n/σ_p ratio due to the presence of this background. after the correction is applied, is estimated to be $\pm 0.2\%$,

B. Elastic *e-d* Scattering Correction

Form factors for the elastic electron-deuteron scattering process were taken from the work of Hartmann.[39] The cross sections at our angles and energies were calculated using these form factors in combination with the appropriate Mott cross sections. The kinematics of the process were such that the elastic electrons were outside of our electron-momentum acceptance for all runs except those at $q^2=7$ and 10 F^{-2}.

Table VIII lists the $e-d$ contributions and the peak locations for our low-momentum-transfer data points. The recoil deuterons at $q^2=7$ and 10 F^{-2} did not have enough energy to reach our coincidence counters, because of the lead absorber placed in front of the counter bank. All electron events from the $e-d$ elastic process are thus to be found in the (e, not p) category. The elastic $e-d$ process had negligible effect upon our final values for the σ_n/σ_p ratio, and for the σ_{pD}/σ_{pH} ratio.

C. Inelastic (N*) Corrections

The inelastic pion-production process was a significant background for the high-momentum-transfer data. An attempt to understand it and then to subtract it out was made, using both the hydrogen data and the theoretical work of Adler.[40] This attempt was not entirely successful.

Adler's theory of the electroproduction process in the region from threshold to the first $N^*(1238)$ resonance is an improvement upon the earlier work of Fubini,

[39] G. Hartmann, Ph.D. thesis, MIT, 1966 (unpublished).
[40] S. Adler, Ann. Phys. (N.Y.) (to be published).

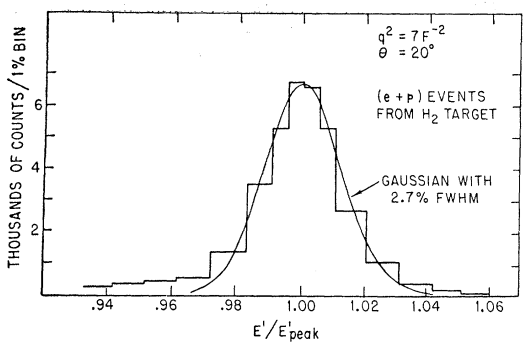

FIG. 14. Scattered electron peak at $q^2=7$ F^{-2} from hydrogen target.

Nambu, and Wataghin.[41] What was done in the present analysis was to generate theoretical scattered-electron spectra for the four possible charge combinations:

$$e+p \rightarrow e+p+\pi^0,$$
$$e+p \rightarrow e+n+\pi^+,$$
$$e+n \rightarrow e+n+\pi^0,$$
$$e+n \rightarrow e+p+\pi^-.$$

The first step was to take the two theoretical cross sections for electroproduction from protons, and to fold their sum with our experimental electron-momentum resolution. The result was then compared to the hydrogen data. Although the predicted shapes of the N^* excitation from hydrogen agreed well with the data, the absolute magnitudes did not agree. In order to obtain good fits, it was necessary to multiply the Adler predictions by factors of 1.7 and 2.2 at $q^2=45$ and 70 F^{-2}, respectively. At lower momentum transfers, not enough N^* excitation entered our acceptance to allow for meaningful comparisons with the theory.

No attempt was made to break down the predicted N^* distributions into events with and events without a coincidence in the proton-counter telescope. The hydrogen electron spectra at $q^2=7$, 45, and 70 F^{-2}, with

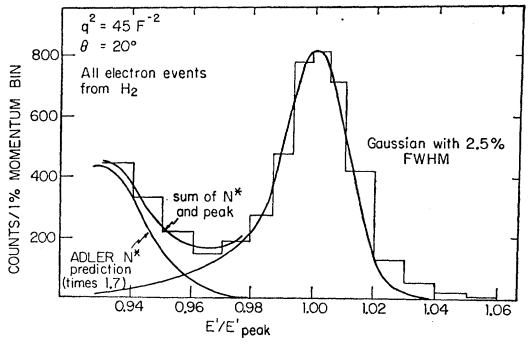

FIG. 15. Scattered electron spectrum at $q^2=45$ F^{-2}, from hydrogen target.

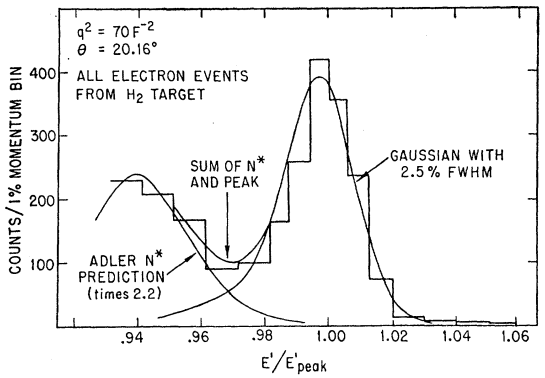

FIG. 16. Scattered electron spectrum at $q^2=70$ F^{-2}, from hydrogen target.

the predicted N^* spectra, are shown graphically in Figs. 14–16. Note that none of the data discussed here are in the region at the very top of the $N^*(1238)$ peak, because only the threshold side entered our momentum acceptance.

To determine the N^* excitation from a deuterium target, contributions from all *four* of the above isotopic spin combinations were summed. The resulting theoretical electron N^* spectrum was then compared to the deuterium data. The electron N^* spectrum was assumed to be spread out in momentum space in exactly the same way as the quasi-elastic peak; that is, the *shape* of the theoretical quasi-elastic peak (determined by the deuteron wave function), a radiative correction, and the experimental *resolution function* were folded in. This attempt to account for the extra smearing because of the initial nucleon momentum inside the deuteron is in fact only the manifestation of the impulse approximation as applied to the pion electroproduction process using a deuteron target.

The results of the comparison between prediction and observation are surprising, as shown in Figs. 17–20.

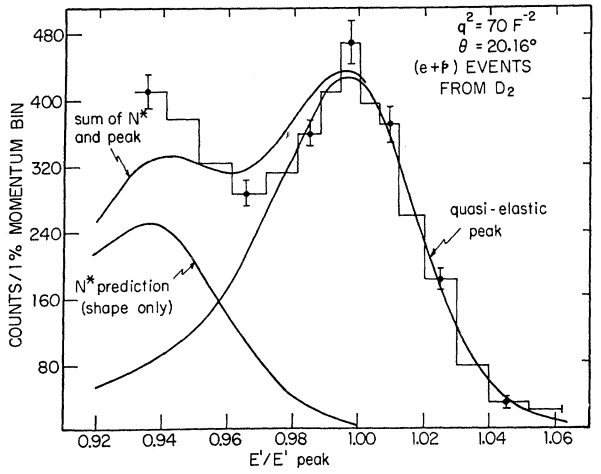

FIG. 17. Scattered electron spectrum with coincident proton from D_2 target, $q^2=70$ F^{-2}.

[41] S. Fubini, Y. Nambu, and V. Wataghin, Phys. Rev. 111, 329 (1958).

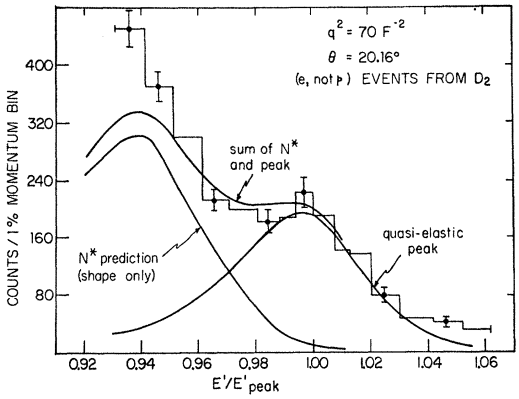

FIG. 18. Scattered electron spectrum without coincident proton from D_2 target, $q^2=70$ F^{-2}.

Even when the Adler predictions for $q^2=45$ and 70 F^{-2} are multiplied by factors of 1.7 and 2.2, respectively (as in the hydrogen case), the fits are not good. At $q^2=45$ F^{-2} (Fig. 19), the total observed N^* excitation area fits well, but the shape is not correct; the data are slightly too high in the valley and too low near the $N^*(1238)$ peak. At $q^2=70$ F^{-2} (Fig. 20), both the magnitude and the shape are in very poor agreement with the data.

Again, for the deuterium targets, no attempt was made to separate the N^* electrons into those events with and those without coincidences in the proton telescope. The statistical precision of our data was such that this separation was unnecessary even at $q^2=70$ F^{-2} where the N^* contamination was most serious. The simplifying assumption was made instead that the fraction of electrons which had coincidences was constant over the entire N^* spectrum; the value of this fraction was taken to be that fraction observed in the very lowest momentum bins, where contamination from quasi-elastic events was smallest. This fraction turned out to be just under 0.50 at the three highest q^2 points. The actual numbers for the ratio $[(e+p)/(\text{all } e)]$ at $q^2=30$, 45, and 70 F^{-2} were 0.44 ± 0.02, 0.42 ± 0.03, and 0.47 ± 0.02, respectively. At the lower q^2 points the value 0.50 was assumed, but N^* production was sufficiently small that the assumption had negligible effect upon our final results.

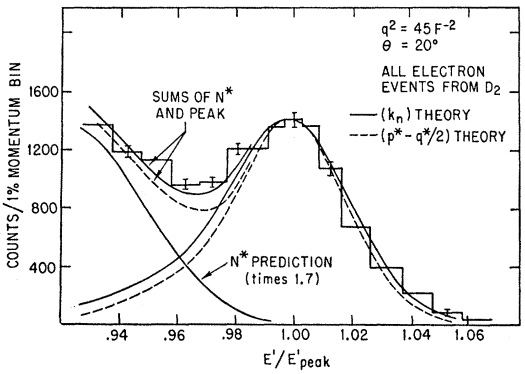

FIG. 19. Total scattered electron spectrum from D_2 target, $q^2=45$ F^{-2}.

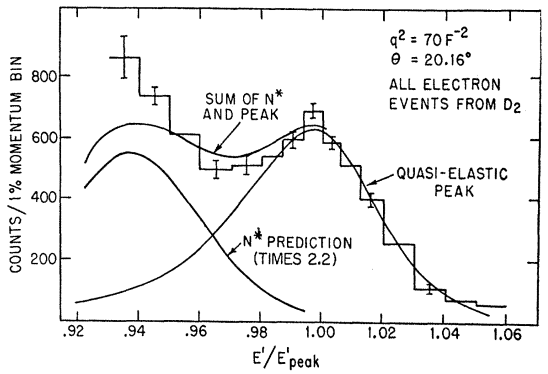

FIG. 20. Total scattered electron spectrum from deuterium target, $q^2=70$ F^{-2}.

D. Electron Peak Shapes from Hydrogen

The peak shapes from elastic electron-proton scattering are a direct measure of our experimental momentum-resolution function, once the radiative tail is unfolded and the target-wall subtraction is made. What was done in this analysis was to perform the unfolding and subtracting of the elastic peak from the hydrogen target and then to use this experimentally measured resolution for analysis of the deuteron data. This procedure avoids the pitfalls possibly present in the use of a calculated resolution. In particular, the observed resolution function changed significantly from run to run because of its sensitivity to the beam spot size. Examples of the hydrogen spectra are shown in Figs. 14–16. The figures show the hydrogen peaks at $q^2=7$, 45, and 70 F^{-2}, respectively.

In order to repeat any of our calculations, the actual momentum resolution function of the system will be required. Folding a Guassian distribution with a theoretical prediction is an entirely adequate approximation for making comparisons with the data. Table IX lists the full width at half-maximum (FWHM) of the Gaussian which best fits the hydrogen data at each momentum transfer. We note, however, that the actual resolution function is slightly wider in the tails than would be given by a Gaussian distribution.

TABLE IX. Gaussian approximations to the measured momentum resolution function.

q^2 (F^{-2})	θ	FWHM of Gaussian (in units of $\Delta E'/E'$)
7	20°	2.7%
10	20°	2.2%
15	20°	2.3%
20	20°	1.9%
30	20°	2.1%
45	20°	2.5%
70	20.16°	2.5%

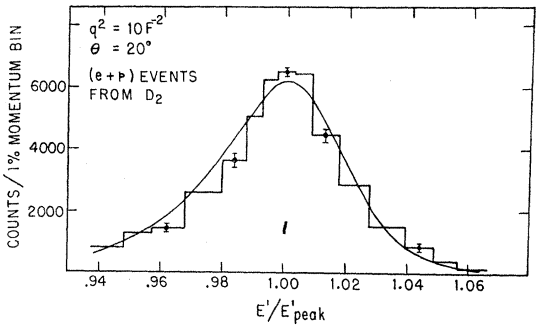

FIG. 21. Scattered electron spectrum with coincident proton from D_2 target, $q^2=10$ F^{-2}.

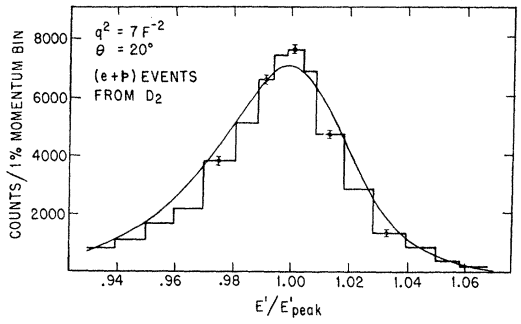

FIG. 23. Scattered electron spectrum with coincident proton from D_2 target, $q^2=7$ F^{-2}.

E. Electron-Momentum Spectra from Deuterium

The procedure for calculating the expected quasi-elastic momentum spectra is to take the theoretical spectra and generate the spectra after radiative corrections are applied. Next, the resolution function, taken directly from the hydrogen data, is folded in. The solid angle subtended by the proton coincidence counter bank is then used to calculate the number of protons not accepted, and the corresponding corrections are applied to the predicted $(e+p)$ and $(e$, not $p)$ spectra separately.

The data are compared with the expected shapes in Figs. 17–25. Figures 17 and 18 show the $(e+p)$ and $(e$, not $p)$ spectra at $q^2=70$ F^{-2}. Figure 20 shows the spectrum of all electrons at $q^2=70$ F^{-2}. In the latter figure, the N^* spectrum according to the Adler theory, but after multiplication by a factor of 2.2 is also shown. It is important to notice that there is excess cross section in the region of the N^* peak (as discussed in the previous section).

Figure 19 shows the spectrum of all electrons at $q^2=45$ F^{-2}. The theoretical spectrum using the "$\mathbf{k}_n$ theory" is shown, as in all of the other cases presented here, but in this figure the prediction of the "$(\mathbf{p}^*-\frac{1}{2}\mathbf{q}^*)$ theory" is also shown, demonstrating that it yields a peak shape slightly narrower than the observed shape. Here, the N^* theoretical shape has been scaled by a factor of 1.7.

Figures 21 and 22 show both the $(e+p)$ and the $(e$, not $p)$ spectra at $q^2=10$ F^{-2}. Note that there is excess $(e$, not $p)$ cross section on the high-energy side of the peak and that only about half of the excess is accounted for by the elastic $e-d$ contribution. However, the $(e+p)$ data seem to agree well with the theoretical prediction on the high-energy side. In the peak region, both peak shapes are slightly narrower than the predicted curves. Figures 23 and 24 show the $(e+p)$ and $(e$, not $p)$ spectra at $q^2=7$ F^{-2}. Again, both peak shapes are *narrower* than the predicted curves in the main peak region. This feature will be commented upon later. There is again significant excess of $(e$, not $p)$ events above the peak, while the $(e+p)$ shape is correctly predicted.

Figure 25 shows the small amount of data at $q^2=115$ F^{-2}, the highest momentum transfer at which data were taken in this experiment. The spectrum seems to fit the predicted peak shape to within the poor statistical precision. Both the quasi-elastic and N^* spectra shown in this figure are scaled arbitrarily for a "best fit" to the data. The statistical precision is too poor to allow for any very meaningful comparisons, and the statement that the fit is adequate is very weak.

Note, however, that the $(e$, not $p)/(e+p)$ ratio is about constant across the spectrum, and about equal to *unity* everywhere. This fact should enable a meaningful σ_n/σ_p ratio to be extracted from the data even though the inelastic (N^*) contamination is quite large. Despite this fact, potential problems might be present in this

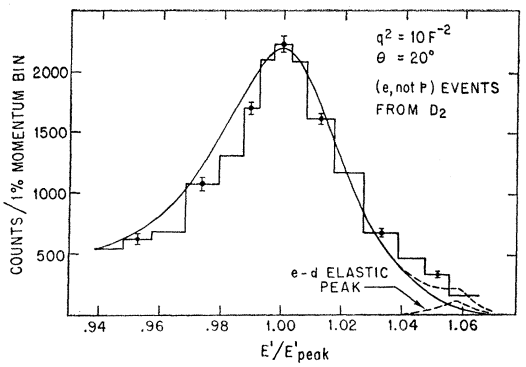

FIG. 22. Scattered electron spectrum without coincident proton from D_2 target, $q^2=10$ F^{-2}.

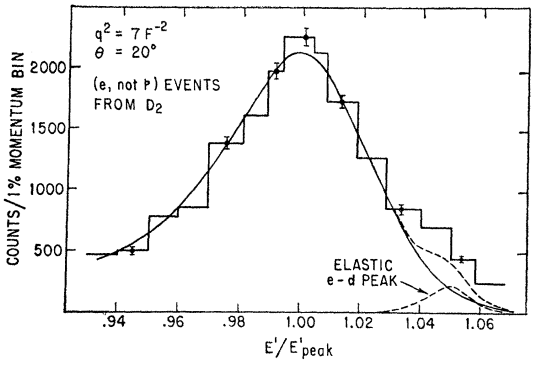

FIG. 24. Scattered electron spectrum without coincident proton from D_2 target, $q^2=7$ F^{-2}.

data, and the best that can be derived from it with certainty is an upper limit on the neutron cross section.

IX. *e-p* CROSS SECTIONS FROM DEUTERIUM AND HYDROGEN

The ratio of the electron-proton cross section from deuterium to that from hydrogen is a measure of how equivalent the "bound proton" inside the deuterium is to the "free proton" in hydrogen.

The $(\sigma_{pD}/\sigma_{pH})$ ratios measured in this experiment are tabulated in Table X. The momentum bite $\Delta E'$ (in percent of the central energy, E'_{peak}) is listed for the hydrogen and deuterium data separately, because at some momentum transfers slightly different bites were used. These data have been corrected for events outside our momentum and angular acceptances. No final-state interactions have been considered.

Our measured σ_{pD}/σ_{pH} ratios are 4%–8% smaller than the expected values at all but the highest momentum-transfer point. This we interpret as a small but significant breakdown of the impulse approximation as we have used it and this will be discussed later.

All theoretical calculations were performed using the modified Hulthén wave-function model, assuming a 5% D-state probability. The fraction of S-state *electrons* missed was determined by integrating the cross section numerically from threshold to the appropriate cutoff, and then continuing down to 30% below E'_{peak}, at which point the cross section had fallen to about 10^{-5} of its peak value. The fraction of S-state *protons* missed was arrived at by folding in the proton-counter solid-angle acceptance with the triply-differential cross section. The small terms were calculated to contribute about 3%–5% to the cross sections within the chosen bites; of these terms, the D-state proton term is the largest.

The radiative corrections, after folding with the experimental resolution function, are tabulated also. The folding introduced about 0.1%–0.2% extra correction, above that which would have been present with extremely fine resolution. The deuterium correction includes the small extra effect due to the difference between the hydrogen and deuterium real bremsstrahlung corrections.

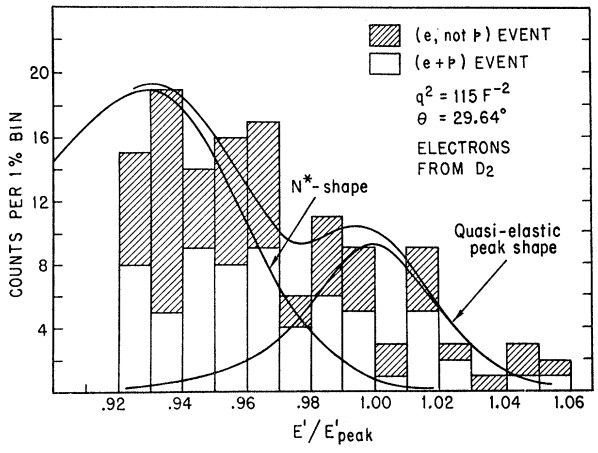

FIG. 25. Scattered electron spectrum from D_2 target, $q^2=115$ F^{-2}.

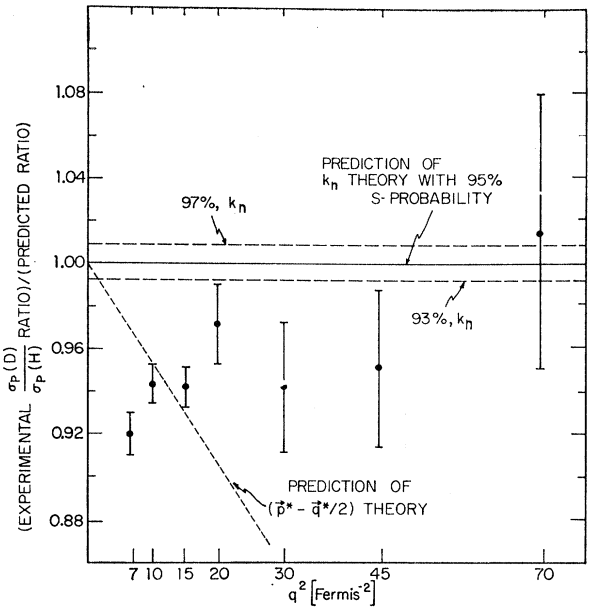

FIG. 26. Comparison between observed and predicted $(\sigma_{pD}/\sigma_{pH})$ ratios.

The $(\sigma_{pD}/\sigma_{pH})$ ratios are shown graphically in Fig. 26. The ratio of observed to predicted proton cross section is plotted, for the "$\mathbf{k}_n$" theory and an assumed 95% S-state probability. Also shown are the predicted ratio for the $(\mathbf{p}^*-\frac{1}{2}\mathbf{q}^*)$ theory, and for the $\mathbf{k}_n$ version with 93% and 97% S-state probabilities. The $\pm 2\%$ change in D-state probability only shifts our predicted (σ_{pD}) values by $\pm 0.8\%$ as discussed earlier.

These ratios, as well as the $(\sigma_{all\ e})$ ratios in Table XI, are extremely sensitive to the radiative-correction values. The δ-function technique used to apply the radiative corrections has already been discussed. If the Meister and Griffy radiative corrections (using cutoff values in the 10-keV region) are applied, the area method deuterium cross sections are reduced by 4–6%, increasing the discrepancies in $(\sigma_{pD}/\sigma_{pH})$.

Except at $q^2=7$ F^{-2}, the proton-absorption correction is the same for the hydrogen and deuterium data, and thus cancels out of the ratio.

X. AREA METHOD (NONCOINCIDENCE) ELECTRON-NEUTRON CROSS-SECTION RATIOS

There are three dominant errors in the σ_{eD}/σ_{eH} ratio: the uncertainty due to counting statistics; the uncertainty in the inelastic (N^*) subtraction; and the uncertainty due to the correction for events not included in the accepted electron momentum bite. To estimate the last uncertainty, the cross section was calculated for

TABLE X. (σ_{pD}/σ_{pH}) ratios.

q^2 (F^{-2})	7	7		10	15	15	20	30	45	45		70
θ	20°	20°		20°	20°	90°	20°	20°	20°	20°		20.16°
Run number	1 of 2	2 of 2		1 of 1	1 of 1	1 of 1	1 of 1	1 of 1	1 of 2	2 of 2		1 of 1
$\Delta E'/E'$ bite D_2	−5.6 to +7.3%	−5.8 to +7.1%	7 20°	−5.2 to +6.6%	−5.7 to +7.1%	−6.9 to +7.0%	−4.2 to +8.0%	−5.8 to +6.5%	−6.3 to +6.6%	−4.3 to +6.8%	45 20°	−3.7 to +7.3%
(% of E'_{peak}) H_2	−6.0 to +6.9%	−5.8 to +7.1%	sum of two runs	−5.2 to +6.6%	−4.6 to +7.2%	−6.9 to +7.0%	−4.7 to +7.5%	−4.8 to +6.5%	−6.3 to +6.6%	−4.6 to +7.5%	sum of two runs	−2.8 to +6.3%
Expected (σ_{pD}/σ_{pH}):												
Size of 95% S-state term	+0.9605	+0.9605		+0.9605	+0.9611	+ 0.969	+0.9615	+0.9621	+0.9623	+0.9623		+0.9647
S-state electrons not in bite	−0.0466	−0.0446		−0.0468	−0.0377	− 0.290	−0.0678	−0.0353	−0.0294	−0.0775		−0.1030
S-state protons lost	−0.0185	−0.0185		−0.0120	−0.0060	− 0.008	−0.0070	−0.0035	−0.0035	−0.0030		−0.0020
Small terms in bite	+0.0292	+0.0292		+0.0365	+0.0389	+ 0.030	+0.0298	+0.0456	+0.0590	+0.0510		+0.0527
Sum of above	0.9246	0.9266		0.9382	0.9563	0.701	0.9167	0.9689	0.9884	0.9323		0.9122
Size of corrections:												
H_2 radiative corr'ns:												
Meister+Yennie	1.1074	1.1095		1.1207	1.1354	1.1040	1.1370	1.1400	1.1192	1.1474		1.1970
Rad. before scatt.	−0.0055	−0.0054		−0.0049	−0.0079	− 0.0162	−0.0092	−0.0113	−0.0189	−0.0130		−0.0091
D_2 radiative corr'ns:												
δ-function	1.1250	1.1229		1.1316	1.1265	1.0953	1.1530	1.1293	1.1221	1.1568		1.1726
Rad. before scatt.	−0.0057	−0.0056		−0.0060	−0.0082	− 0.0175	−0.0069	−0.0120	−0.0162	−0.0106		−0.0112
($\delta_{III}+\delta_{II}$)	+0.0005	+0.0005		+0.0014	+0.0024	+ 0.0151	+0.0031	+0.0044	+0.0044	+0.0064		+0.0113
H_2 N^* subtraction	...	...		...	...	...	0.10%	0.40%	9.0%	2.4%		1.9%
D_2 N^* subtraction	...	...		...	0.27%	...	0.01%	3.15%	14.1%	8.1%		14.6%
Cross sections:												
Observed (σ_{pD}/σ_{pH})	0.854	0.850		0.884	0.900	0.719	0.890	0.912	0.883	0.899		0.926
Ratio: (observed/expected)	0.924	0.917	0.919	0.943	0.941	1.026	0.971	0.941	0.894	0.964	0.950	1.015
Fractional errors:												
Statistical error	±1.33%	±0.89%	±0.74%	±1.08%	±1.11%	±12.2%	±1.9%	±3.0%	±4.7%	±2.3%	±2.1%	±4.9%
Uncertainty due to $\Delta E'/E'$ cutoff	0.50%	0.50%	0.50%	0.25%	0.20%	4.0%	0.5%	0.4%	0.3%	2.0%	2.0%	3.0%
N^* correction error	...	...	...	...	...	...	...	1.0%	3.0%	2.0%	2.3%	3.0%
Net (in quadrature)	±1.42%	±1.04%	±0.89	±1.10%	±1.13%	±13.2%	±1.96%	±3.19%	±5.6%	±3.7%	±3.6%	±6.5%

several different cutoff points, both greater than and less than the cutoff finally chosen. At every momentum transfer, consistency in the final cross section (within the statistical precision) was achieved over a range of 2–3% in the cutoff. The error attributed to the cutoff is an estimate of the remaining uncertainty. It is largely due to the uncertainty in the actual absolute value of $\Delta E'$, due to uncertainties in the calibration of our counter momentum-bin sizes. Another contributing factor is the uncertainty in the folding of experimental resolution with the S-state electron spectrum. The estimated uncertainty in the inelastic (N^*) contamination is based on both the inability to predict correctly the N^* contamination in deuterium, and the possibility that our assumption about the constancy of the $[(e+p)/(\text{all } e)]$ ratio over the N^* peak is incorrect.

Table XI tabulates the ratio of the cross section for *all deuterium electrons* to that for *all hydrogen electrons*. These cross sections were determined using the same cutoffs in E' as are listed in Table X for the $(\sigma_{p\mathrm{D}}/\sigma_{p\mathrm{H}})$ cross-section ratios. The small terms correction is different in this case, however, since it must take into account the (e, not p) electrons from the small terms. Also, the elastic $e-d$ events, another (e, not p) process, must be subtracted out. However, there are *no* corrections for any processes associated with the coincidence counters, since these cross sections only involve detection of the scattered electron.

XI. σ_n/σ_p COINCIDENCE-METHOD RATIOS

Variation of the σ_n/σ_p Ratios with Scattered Electron Energy

According to the theoretical calculations outlined above, there should not be a very significant variation of the σ_n/σ_p ratio across the quasi-elastic peak. A small and well-understood variation exists, due to the q^2 dependence of the form factors; it amounts in the worst case ($q^2=7$ F^{-2}) to about $\pm 0.3\%$ change in σ_n/σ_p for $\pm 1\%$ change in E'.

However, the measured (e, not p)/($e+p$) ratios show a significant variation for every q^2 point in this experiment, even after all *experimental* corrections (chance rate; neutron conversion; proton absorption; radiative corrections) and background subtractions (elastic $e-d$; inelastic N^* contamination) are applied. This variation is partially but not entirely understood using the deuteron theory. There are two theoretical corrections to be applied: that due to missed S-state protons, thrown outside of the proton counter acceptance; and that due to the other (small) terms. Both of these effects alter the ($e+p$) and (e, not p) cross sections by different amounts at different E' values across the quasi-elastic peak.

In Figs. 27–32 the variation of the σ_n/σ_p ratio with E is shown for some of the various momentum-transfer points in this experiment.

At all points, the ratio is displayed both before and

TABLE XI. $[\sigma_{\mathrm{all}\,e^-}(\mathrm{D})/\sigma_{\mathrm{all}\,e^-}(\mathrm{H})]$ ratios.

q^2 (F^{-2})	7	7	7	10	15	15	20	30	45	45	45	70
θ	20°	20°	20°	20°	20°	90°	20°	20°	20°	20°	20°	20.16°
Run number	1 of 2	2 of 2	sum of two runs	1 of 1	1 of 1	1 of 1	1 of 1	1 of 1	1 of 2	2 of 2	sum of two runs	1 of 1
Cross-section ratio:												
$[\sigma_{\mathrm{all}\,e^-}(\mathrm{D})/\sigma_{\mathrm{all}\,e^-}(\mathrm{H})]$	1.184	1.185	1.184	1.239	1.263	1.637	1.353	1.379	1.348	1.415	1.395	1.458
Errors in ratio:												
Statistical error	±1.26%	±0.85%	±0.70%	±1.03%	±1.05%	±11.7%	±1.83%	±2.75%	± 4.44%	± 2.90%	±2.43%	± 4.87%
Uncertainty due to $\Delta E'/E'$ cutoff	0.50%	0.50%	0.50%	0.25%	0.20%	4.0%	0.5%	0.4%	0.3%	2.0%	2.0%	3.0%
N^* correction error	...	...	...	...	...	...	...	1.1%	4.0%	2.5%	3.0%	5.0%
Net (in quadrature)	±1.35%	±0.99%	±0.86%	±1.06%	±1.08%	±12.4%	±1.91%	±3.00%	± 5.98%	±4.32%	±4.35%	±7.6%
Corrections to raw data:												
S-state electrons not in $\Delta E'/E'$ bite	+4.66%	+4.46%		+4.68%	+3.77%	+29.0%	+6.78%	+3.53%	+ 2.94%	+ 7.75%		+10.30%
Small-term electrons in bite	−3.17%	−3.17%		−3.45%	−4.07%	− 4.0%	−3.81%	−4.92%	− 4.90%	− 4.90%		− 5.05%
N^* subtraction to D data	...	...		−0.03%	−0.39%	...	−0.02%	−4.2%	−22.6%	−11.0%		−23.6%
Elastic e-D subtraction	−1.15%	−1.15%		−0.45%	−0.15%	...	...	...	...	...		...

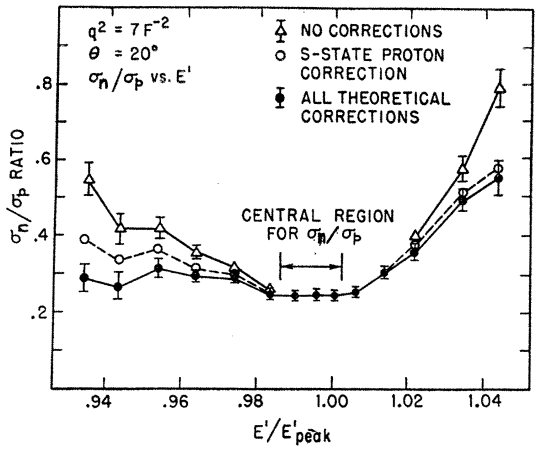

FIG. 27. (σ_n/σ_p) ratios versus E' at $q^2=7$ F^{-2}.

after the deuteron-theory corrections are applied. However, all experimental corrections such as chance rate, empty target, and n-p conversion, have already been made. At the higher momentum transfers, the values before and after the N^* subtraction is made are also shown. On each figure the region in E' is indicated which was eventually chosen for analysis to determine the "final" σ_n/σ_p ratio value.

If the theory were entirely correct in its predictions, the ratios would all lie on a straight line at each q^2, after the application of all corrections. It can be seen that this is true within the statistical precision over most of the peak region for the higher momentum transfers. For example, the graph for the $q^2=70$ F^{-2} point shows that the N^* subtraction, combined with the theoretical corrections, brings the points into a straight line to within the (unfortunately large) statistical fluctuations.

At the lower momentum transfers, however, there still remains significant variation, especially on the high (threshold) side of the peak. The elastic e-d subtraction

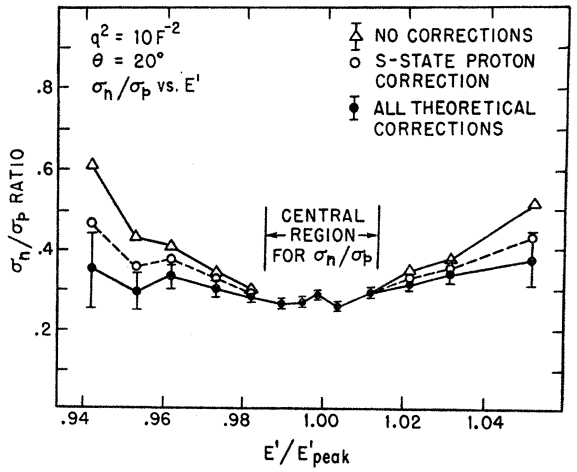

FIG. 28. (σ_n/σ_p) ratios versus E' at $q^2=10$ F^{-2}.

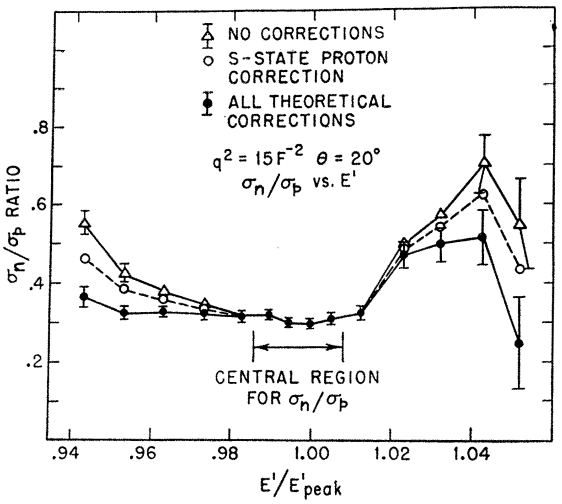

FIG. 29. (σ_n/σ_p) ratios versus E' at $q^2=15$ F^{-2}, $\theta=20°$.

is already made in the plots at $q^2=7$ and 10 F^{-2}, but it is not sufficient in either case to bring down the σ_n/σ_p ratios to the central values. This was also observed in the discussion of the electron peak shapes, where an excess of (e, not p) events was present for both $q^2=7$ and 10 F^{-2}.

The method used in this analysis is to take the values for σ_n/σ_p from the data at the top of the quasi-elastic peak. A demonstration that the rest of the peak is also understood is important because it gives additional confidence in the analysis procedure. Also, if the σ_n/σ_p ratio is constant after all corrections are applied, then there is little sensitivity to the actual $\Delta E'$ momentum bite chosen for the final σ_n/σ_p analysis.

The E' bite chosen at the lowest momentum transfers was determined by the criterion that a bite significantly

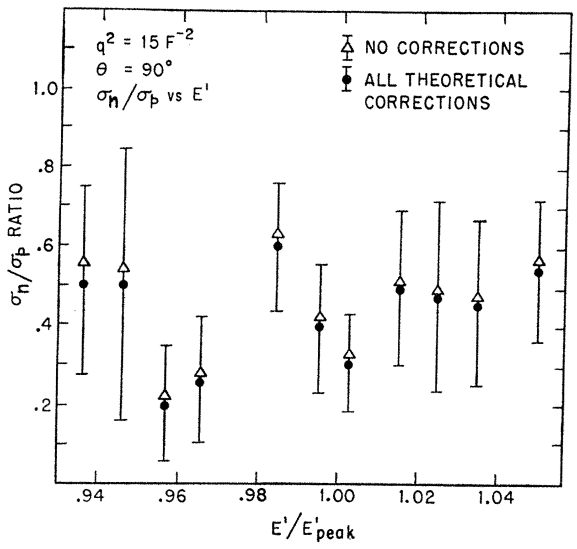

FIG. 30. (σ_n/σ_p) ratios versus E' at $q^2=15$ F^{-2} at the backward scattering angle (90°).

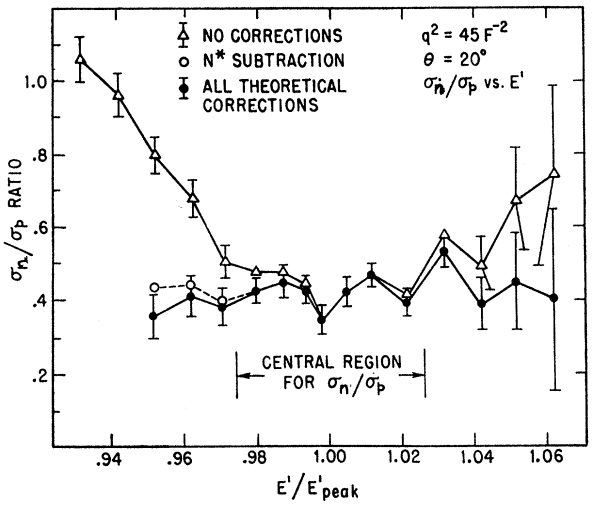

FIG. 31. (σ_n/σ_p) ratios versus E' at $q^2=45$ F^{-2}.

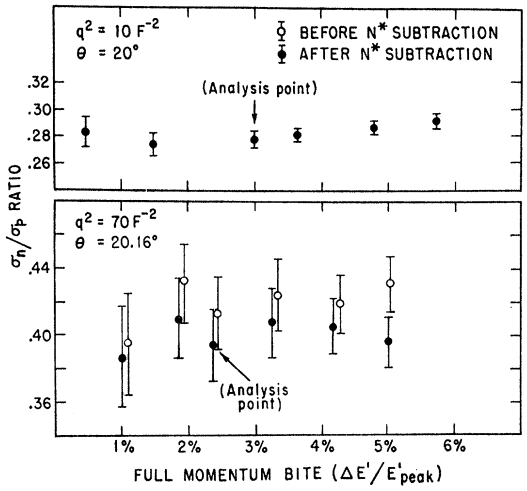

FIG. 33. (σ_n/σ_p) ratios for various momentum acceptances, $\Delta E'/E'$, about the quasi-elastic peak center.

smaller than the intrinsic momentum resolution of the system was not sensible, while a bite large enough to include much sensitivity to the tails region was also undesirable. For the higher momentum transfers, it was also desirable to avoid N^* contamination if possible, which precluded a bite very wide on the low-momentum side of the peak.

Figure 33 shows the average σ_n/σ_p ratio for increasingly larger $\Delta E'$ bites about the peak center, for two cases. The bite chosen for eventual analysis is indicated in each case. We note that the average σ_n/σ_p ratio at $q^2=10$ F^{-2} is not significantly altered by expanding the electron momentum acceptance even though the ratio shows significant variation. This is because there are relatively fewer events in the additional momentum bins. Improved momentum resolution would have been helpful here.

We display in Fig. 34 the summary of σ_n/σ_p derived from coincidence data at the top of the quasielastic peak (Table XII). We also include σ_n/σ_p derived from the data on the electron spectrum alone according to the simple prescription

$$\sigma_n/\sigma_p=\sigma_{eD}/\sigma_{eH}-1.$$

Also, on the plot are data from other authors with slight kinematic adjustments to our experimental conditions and the curves from the prescriptions of the scaling law

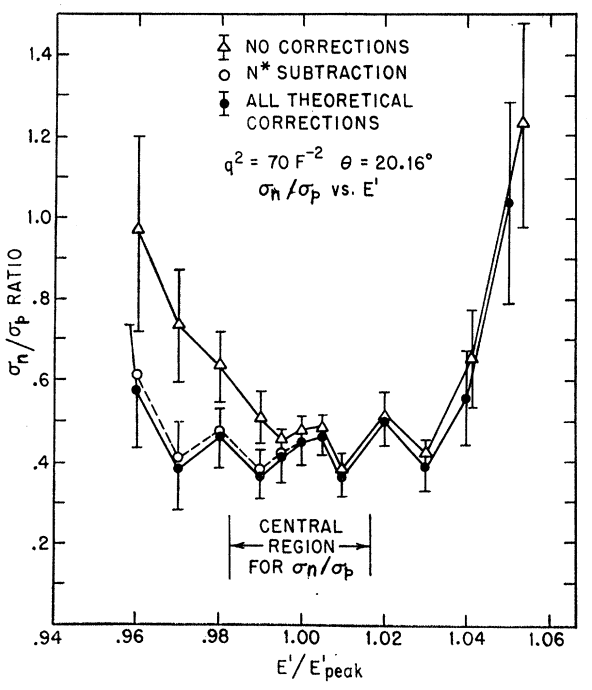

FIG. 32. (σ_n/σ_p) ratios versus E' at $q^2=70$ F^{-2}.

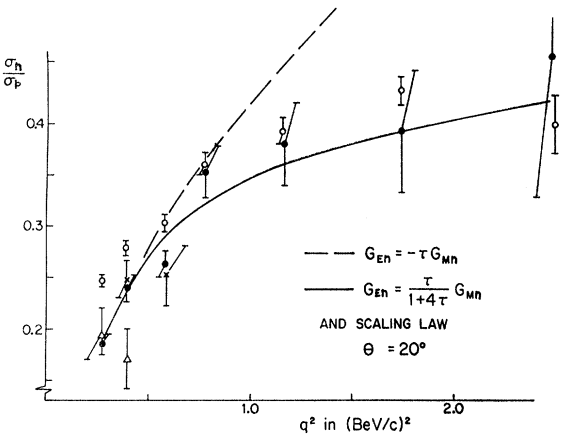

FIG. 34. σ_n/σ_p derived from coincidence data (open circles) and area-method analysis of noncoincidence data (dark circles). Also shown for comparison are extrapolated values for σ_n/σ_p from the 45° data of Hughes (Ref. 13) (open triangles) and the 55° and 35° data of Stein (Ref. 17) (crosses). The dashed curve is derived from the scaling-law prediction: $G_{Ep}=G_{Mp}/\mu_p=G_{Mn}/\mu_n$ and $G_{En}=-\tau G_{Mn}$. The solid line assumes the scaling law $G_{En}=[-\tau/(1+4\tau)]G_{Mn}$.

derived later in Sec. XIV. We note here that the coincidence data are systematically higher than the noncoincidence data. Moreover, they lie well above reasonable extrapolations of the neutron-electron interaction: $G_{En}=-\tau G_{Mn}$. This point will be discussed further in Sec. XIV.

XII. RECOIL PROTON ANGULAR DISTRIBUTIONS

Information about the angular distribution of recoil protons was obtained by the use of a 12×12 (144-bin) checkerboard hodoscope. It was placed behind two (or sometimes three) counters, which served to detect the recoil protons. The layout was arranged so that any particle trajectory originating in the target and passing through the hodoscope must have traversed the trigger counters.

Two features degraded the usefulness of the hodoscope information. The first was the large background counting rate in the individual hodoscope scintillators. The second was the fact that at the lower momentum transfers ($q^2=7$, 10, and 15 F^{-2}), lead absorber was used in order to shield the proton counters from background. The multiple scattering in the lead was important in degrading the angular resolution; also, the range limitation due to the lead prevented studies in some kinematic regions.

A. Analysis of the Hodoscope Data

The analysis of the hodoscope data was performed in the following manner: Any event with one and only one counter firing in each hodoscope plane was termed a "good" event. An event with all hodoscope counters off was termed an "empty" event. All other hodoscope patterns were called "other" events. Only the "good" category was used in the final analysis of the data, because there was no way to assign the "other" events. Thus only a relative distribution of a sample of all events is available for comparison with the theory. Because the sample is not a purely random one, it is crucial to demonstrate that the corrections applied to the "good" sample are understandable and introduce negligible error into the final conclusions.

The method used to make this check was to predict the distribution of "other" events from both the assumed parent "good" distribution and the background processes. At one data point ($q^2=20$ F^{-2}), an event-by-event analysis of the "other" events was performed; it revealed that their distribution was indeed consistent with our expectations to within the statistical precision of the data.

An important experimental monitor of the hodoscope's performance is the chance probability. For some of our data points, this was checked by a "delayed" run (in which the hodoscope counter pulses were electronically delayed outside of the true coincidence resolving time). Whenever a "delayed" run was taken, the information it contained was found to be identical to that contained in the analysis of those events in the main run, where the proton coincidence was absent. This latter analysis was therefore used as a measure

TABLE XII.

q^2 (F^{-2})	7	7		10	15	20
θ	20°	20°	7 20°	20°	20°	20°
Run number	1 of 2	2 of 2	sum of	1 of 1	1 of 1	1 of 1
Full $\Delta E'/E'$ bite (% of E'_{peak})	−0.71 to +0.80%	−0.86 to +0.65%	two runs	−1.33 to +1.68%	−1.30 to +0.78%	−2.3 to +3.7%
Experimental corrections:						
Chance rate	1.76±0.10%	1.44±0.10		1.83±0.08%	1.76±0.08%	3.23±0.16%
n conversion	0.68±0.10%	0.68±0.10%		0.77±0.15%	0.74±0.15%	0.20±0.04%
p absorption:						
fraction of p's	4.47±0.29%	4.58±0.24%		5.30±0.24%	4.94±0.25%	1.22±0.55%
% reduction in n/p	18.6 ±1.44%	19.4 ±1.22%		20.2 ±1.10%	19.0 ±1.07%	4.53±2.07%
N^* subtraction,						
% reduction in n/p	...	...		...	...	...
Theoretical corrections:						
S-state proton losses:						
fraction of p's lost	0.35±0.10%	0.40±0.10%		0.40±0.15%	0.15±0.05%	0.55±0.15%
% decrease in n/p	1.74±0.49%	2.04±0.51%		1.84±0.69%	0.64±0.20%	2.07±0.56%
Other small terms:						
% decrease in n/p	0.50±0.15%	0.51±0.15%		0.92±0.34%	1.07±0.41%	0.63±0.25%
Radiative correction:						
($\delta_{II}+\delta_{III}$)	0.25%	0.25%		0.35%	0.40%	0.45%
Cross-section ratios:						
(σ_n/σ_p) after experimental corrections	0.258	0.250	0.253	0.286	0.309	0.376
(σ_n/σ_p) after all corrections	0.251	0.243	0.246	0.278	0.303	0.361
Errors in σ_n/σ_p:						
Fractional:						
Statistical error	±3.9%	±2.9%	...	±2.1%	±2.5%	±2.8%
Other errors	1.5%	1.4%	...	1.4%	1.2%	2.2
Net error (in quadrature)	4.3%	3.2%	±2.5%	2.5%	2.8%	3.6
Absolute error in σ_n/σ_p	...	...	±0.0063	±0.0069	±0.0085	±0.0130

of the background spectrum for those runs in which a "delayed" run was not taken.

The hodoscope scintillators were aligned in a flat plane. There was thus a small probability that a good trajectory could pass through both of two adjacent scintillation slats. No correction to the raw data has been applied for this effect.

The hodoscope data were also used to study the distribution of protons from hydrogen. This angular distribution (for elastic scattering) should correspond to the folding of the multiple Coulomb scattering of the elastic protons with the finite cone of protons due to the electron aperture size and the target-length effect. For the hydrogen runs, *complete consistency* was found between the expected and observed proton distributions, taking into account all known effects.

For the deuterium data, the hodoscope analysis took into account small nonuniformities in the sweeping magnet field. Before the data were compared with the theoretical predictions, corrections were applied to subtract out both events from the target end-walls (measured by an empty-target run), and events where a genuine proton was actually absent although the trigger counters fired accidentally.

B. Calculation of Theoretically Predicted Hodoscope Distribution

The theoretical angular distribution of recoil protons has already been discussed. The distribution has azimuthal symmetry about the direction of the momentum-transfer vector (for any particular set of incident and scattered electron energies E and E', and fixed scattering angle θ). The experimentally observed distribution, however, is not as simple. First, the presence of a range of scattered electron energies implies a folding of a continuum of cones onto the hodoscope plane, the cone for each E' having its own semivertical angle, its own cross-section weighting, and its own central point of impact. The presence of real and virtual bremsstrahlung must be accounted for in a similar way, since any $\Delta E'$ bite

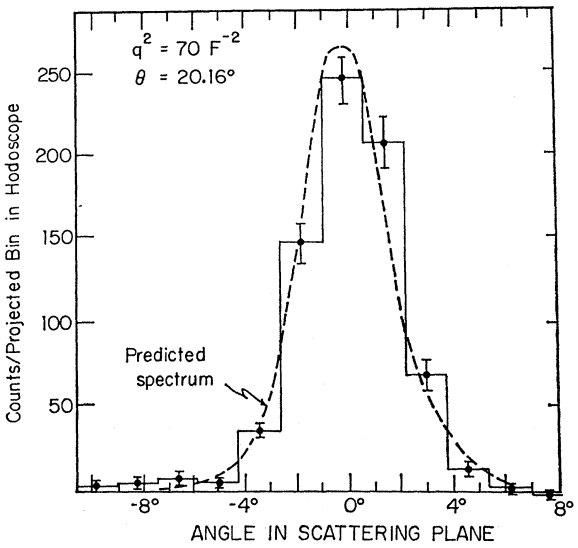

FIG. 35. Proton angular distribution projected onto scattering plane, $q^2 = 70$ F^{-2}.

(σ_p/σ_p) ratios.

30 20° 1 of 3 −2.8 to +2.5%	30 20° 2 of 3 −3.0 to +3.0%	30 20° 3 of 3 −3.0 to +2.3%	30 20° sum of three runs	45 20° 1 of 2 −2.4 to +2.9%	45 20° 2 of 2 −2.3 to +2.7%	45 20° sum of two runs	70 20.16° 1 of 1 −1.03 to +1.80%	115 29.64° 1 of 1 −7.0 to +7.0%	15 90° 1 of 1 −5.9 to +6.0%
4.8 ±0.5% 0.20±0.04%	3.7 ±0.6% 0.20±0.04%	7.2 ±0.4% 0.20±0.04%		4.42±0.52% 0.20±0.04%	6.02±0.20 0.20±0.04		4.71±0.28% 0.20±0.04%	6.2±0.5% 0.2±0.04%	2.6 ±1.0% 1.20±0.25%
3.0 ±1.2% 9.5 ±3.8%	3.0 ±1.2% 10.0 ±4.0%	4.22±0.61% 13.3 ±1.92%		1.78±1.53% 5.91±5.08%	1.24±0.42% 3.90±1.32%		4.89±0.99% 15.2 ±2.9%	4.0±2.0% 8.0±4.0%	7.2 ±1.0% 20.4 ±3.4%
...	...	...		2.0 ±0.7%	1.8 ±0.6%		4.0 ±2.0%	unknown	...
0.40±0.08% 1.38±0.27%	0.40±0.08% 1.33±0.26%	0.45±0.15% 1.42±0.47%		0.08±0.02% 0.30±0.06%	0.08±0.02% 0.30±0.06%		0.15±0.05% 0.45±0.15%	 (estimate)	0.4 ±0.1% 1.3 ±0.3%
0.69±0.13%	0.67±0.13%	0.63±0.25%		0.60±0.20%	0.60±0.20%		0.50±0.20%	2.0±1.0%	3.4 ±0.9%
0.55%	0.55%	0.55%		0.65%	0.65%		0.70%	1.3%	1.60%
0.419 0.408	0.407 0.397	0.405 0.394	 0.396	0.404 0.398	0.449 0.440	 0.435	0.397 0.390	... 0.97	0.439 0.418
±8.5% 3.8 9.4 ...	±7.5% 4.1 8.6 ...	±3.8% 2.0 4.3 ...	 ±3.6% ±0.0142	± 8.5% 5.2% 10.0% ...	±3.2% 1.5% 3.5% ...	 ±3.3% ±0.0145	±7.5% 3.5% 8.3% ±0.0326	22% unknown >22% ...	±14.3% 3.7% 14.8% ±0.0628

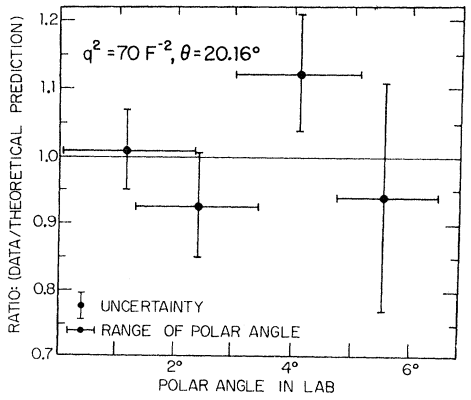

FIG. 36. Ratio of data to predicted polar spectrum for the recoil protons at $q^2=70$ F^{-2}.

contains some electrons which, in the absence of radiation, would have appeared elsewhere in the scattered energy spectrum. Second, the effect of the finite electron aperture and of the finite target length must be folded in. Third, the multiple scattering of the protons in their flight path from target to hodoscope must be accounted for.[42] Finally, the energy dependence of proton absorption can distort the observed spectrum (although this was significant only at the lowest momentum transfer points).

C. Comparison of Hodoscope Data with Theory

The comparison of the data with theoretical predictions will be made in two forms: The observed distribution will in some cases be projected onto a plane, and in other cases be treated as a polar distribution about the central momentum transfer ($\mathbf{q}_v$) direction.

Before presenting the actual data, attention should be drawn to two points. First, the full width of the intrinsic angular resolution was approximately one hodoscope bin for those points ($q^2=20$ F^{-2} and up) in which the sweeping magnet was used. At the lower momentum transfers ($q^2=7$, 10, and 15 F^{-2}) the presence of multiple scattering in the lead absorber increased the resolution to about 2.5 bins (full width). Second, the presence of the lead absorber had an unfortunate consequence: the elimination of protons with energies less than 115 MeV because of a *range* limitation.

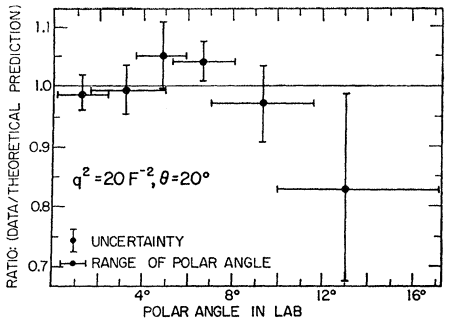

FIG. 37. Ratio of data to predicted polar spectrum for recoil protons, $q^2=20$ F^{-2}.

[42] H. Bethe, Phys. Rev. 89, 1256 (1953).

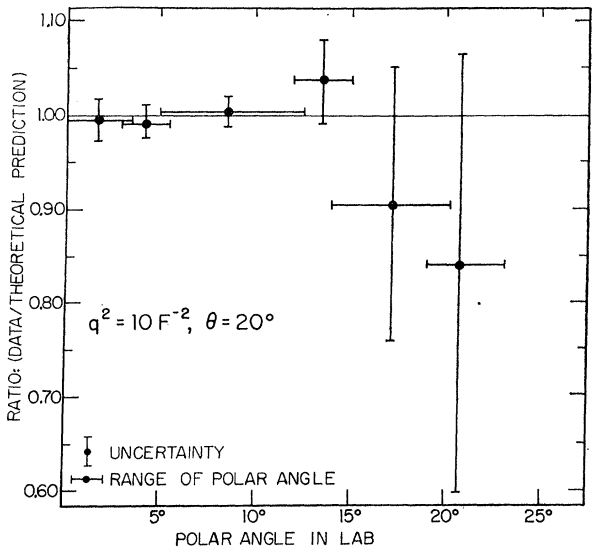

FIG. 38. Ratio of data to predicted polar spectrum for the recoil protons at $q^2=10$ F^{-2}.

At $q^2=7$ F^{-2} a cutoff occurred at electron energies of about $(1.02)E'_{\text{peak}}$; at higher values of E', the energy transfer was so small that the protons all stopped before reaching the hodoscope.

The comparisons with the theoretical predictions are shown in Figs. 35–42. Figures 35–37 show the $q^2=70$ F^{-2} and $q^2=20$ F^{-2} data, respectively. Only protons associated with electrons near the top of the quasi-elastic peaks are included here. Figure 35 shows the distribution projected downward onto the scattering plane, while Figs. 36 and 37 show the comparisons between data and theory as a function of the laboratory polar angle. There is full agreement, with no signs of any discrepancies within the statistical precision of the data for $q^2>20$ F^{-2}. Figures 38–40 show the $q^2=10$ F^{-2} hodoscope data. Figure 38 demonstrates that at the top of

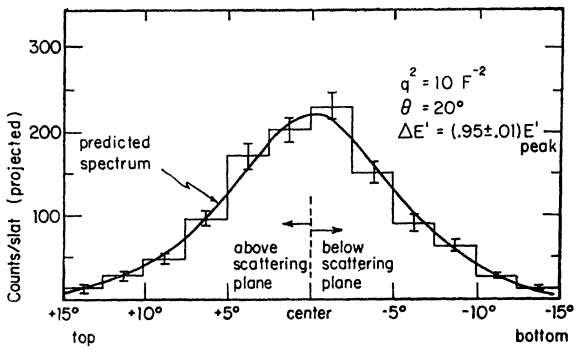

FIG. 39. Proton angular distribution projected sideways, $q^2=10$ F^{-2} for electrons below the peak position.

the quasi-elastic peak the radial (polar) distribution is adequately predicted by the theory. Figure 39 is for electrons *below* the peak, in the region $\Delta E' = (0.95 \pm 0.1)E'_{\text{peak}}$. The distribution shown is projected sideways, so that the left-hand side of the figure shows data above the scattering plane. Again, agreement is obtained between theory and experimental data. Figure 40 shows the hodoscope data for electrons *above* the quasi-elastic peak, in the region $\Delta E' = (1.04 \pm 0.1)E'_{\text{peak}}$. The hodoscope is shown schematically as it would be seen looking from the target. Both the upward and sideways projections are plotted, and there are *statistically significant discrepancies* in both projections. However, a detailed study revealed no correlation between the two projections, within the limited statistics. The up-down asymmetry in the data, which is not understood, is probably due to some unknown instrumental effect. Also, the predicted curve for the upward projection shows that the peak in the distribution is expected to be shifted to larger scattering angles. This shift is due to the change in the direction of the momentum-transfer vector ($\mathbf{q}_v$) for E' values away from the peak. Figure 40 shows that the observed shift is not as great as predicted.

Figures 41 and 42 show the observed and predicted spectra at $q^2 = 7$ F^{-2}. Figure 41 displays both upward and sideways projections for electrons at the top of the peak, while Fig. 42 shows a left-right hodoscope projection for electrons below the peak. Note that in every case the data fall *below* the predicted spectral shape in the tails region (which corresponds to large proton angles away from $\mathbf{q}_v$). No hodoscope data is available at $q^2 = 7$ F^{-2} for electrons above the peak, because of the 115-MeV range limitation on the protons. The energy (range) cutoff was properly taken into account in the $q^2 = 7$ F^{-2} analysis for electrons at the top of the peak, and also in the $q^2 = 10$ F^{-2} analysis; in these cases, it had no significant effect upon the comparison between data and prediction.

In summary, the hodoscope data for electrons near the top of the quasi-elastic peak is correctly predicted by the theory for the $q^2 = 10$–70 F^{-2} points. However, the data at $q^2 = 7$ F^{-2} show fewer protons in the tail region, both on and below the peak. Below the peak, the $q^2 = 10$ F^{-2} data is adequately predicted, while above the peak the $q^2 = 10$ F^{-2} data show significant asymmetries.

XIII. DISCREPANCIES BETWEEN THE DATA AND THEORY

In this experiment we have attempted not only to determine the cross sections of interest, but also to investigate some details of the theory needed to interpret the results. In the course of this investigation, significant discrepancies have been observed between theoretical predictions and our observations. These discrepancies call into question the ability to interpret the data with a reliability comparable to the precision with which the measurements were made.

Discrepancies are largest at the low-momentum-transfer points (7 and 10 F^{-2} in particular) and tend to decrease or disappear at increasingly large momentum transfers, although the statistical precision necessary to investigate them in detail deteriorates at the larger momentum transfers. Four broad categories of disagreement are observed:

(a) The observed angular distribution of recoil protons is slightly narrower than predicted by theory.

(b) The energy spectrum of scattered electrons is narrower than predicted by theory.

(c) The cross section for e-p coincidences (from deuterium), integrated over all proton recoil angles and scattered electron energies, is approximately 5% smaller than the corresponding cross section using a hydrogen target.

(d) The noncoincidence cross sections agree with our preconceptions about the neutron form factors better than do the coincidence data (see Fig. 34).

We will suggest three theoretical frameworks within which to discuss these discrepancies.

(a) First, the presence of final-state interactions in the n-p system will lead to a modification of the impulse approximation. We have not applied any such corrections to our data. Estimates of the final-state interactions at our (relatively high) momentum transfers have been made by McGee,[4] who treats the spectator nucleon as a partially absorbing disk. This approach leads to an equal depression of *both* the neutron and proton cross sections, thus leaving the ratio (σ_n/σ_p), as measured by a coincidence technique, unaltered. McGee predicts a reduction in the doubly-differential cross section of about 8.5% *on the top of the quasi-elastic peak*, relatively independent of momentum transfer for sufficiently high momentum transfers. This result is in qualitative agreement with the observed 5% reduction of $\sigma_{p\text{D}}$ by comparison with $\sigma_{p\text{H}}$ which is relatively independent of q^2 at and above 10 F^{-2} (see Fig. 26). The 5% reduction is, however, obtained by integrating over the quasi-elastic peak. McGee also predicts a narrowed triply-differential cross section $(d^3\sigma/d\Omega_p d\Omega dE')$ which is in agreement with our observations.

However, McGee's final-state calculation in its present form does not explain the most important discrepancy which we observe: The σ_n/σ_p ratios derived from the coincidence data give values much too high to be in agreement with the slope of the neutron electric form factor at small momentum transfers (see Fig. 34). Moreover, the same type of calculation should apply to quasi-elastic proton-deuteron scattering and would predict that the doubly differential p-d cross sections should be reduced no more than the total cross sections. As discussed below, this is in disagreement with experiment. Clearly, more calculations are needed.

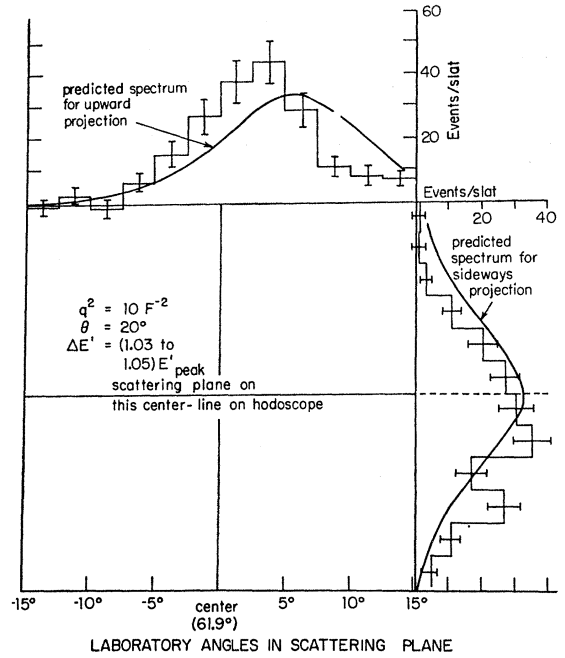

FIG. 40. Proton angular distributions projected upward and sideways, $q^2=10$ F^{-2}, for electrons above the peak position.

(b) In the second approach, we compare the quasi-elastic *e-d* scattering with measurements of proton-deuteron quasi-elastic scattering:

$$p+d \rightarrow p+p+n,$$

which are susceptible to similar final-state interactions. In experiments[43] performed at 150 MeV, in which both

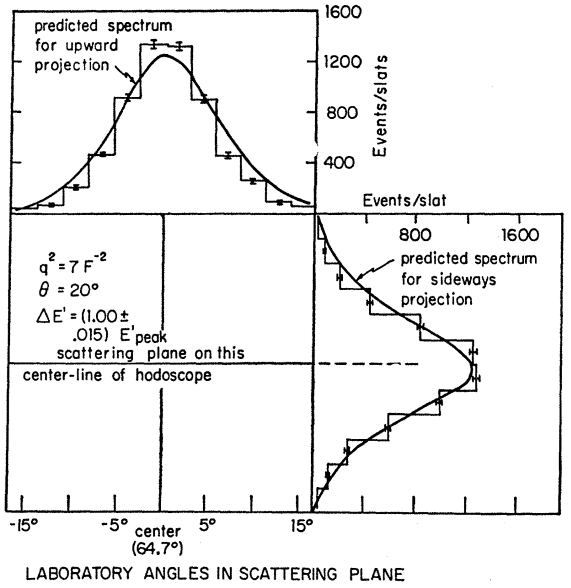

FIG. 41. Proton angular distributions projected upward and sideways, $q^2=7$ F^{-2}, for electrons near the peak position.

[43] A. E. Kuckes, Richard Wilson, and P. F. Cooper, Jr., Ann. Phys. (N.Y.) **15**, 193 (1961).

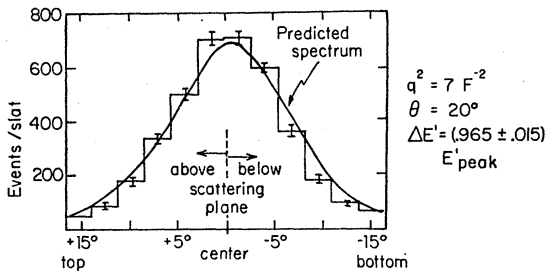

FIG. 42. Proton angular distribution projected sideways, $q^2=7$ F^{-2}, for electrons below the peak position.

final-state protons were detected, features very similar to those noted above for *e-d* scattering were observed, although the discrepancies were much larger. In particular, the discrepancy between the *p-d coincidence* data and the known *p-p* elastic cross section was about 20%, while the noncoincidence *p-d* data differed by only about 10% from the sum of the known *p-p* and *n-p* cross sections. The *total p-d* cross section (integrated over angles of both the outgoing protons) agreed with the sum of the proton-proton and neutron-proton total cross sections better still, to within approximately 3%.

An attempt was made to explain these *p-d* experiments by taking the ratio of measured to calculated cross sections (always less than unity) and extrapolating to the nucleon pole, where the impulse approximation should be exact. Qualitative agreement was obtained.[44] An attempt to treat the present quasi-elastic *e-d* data

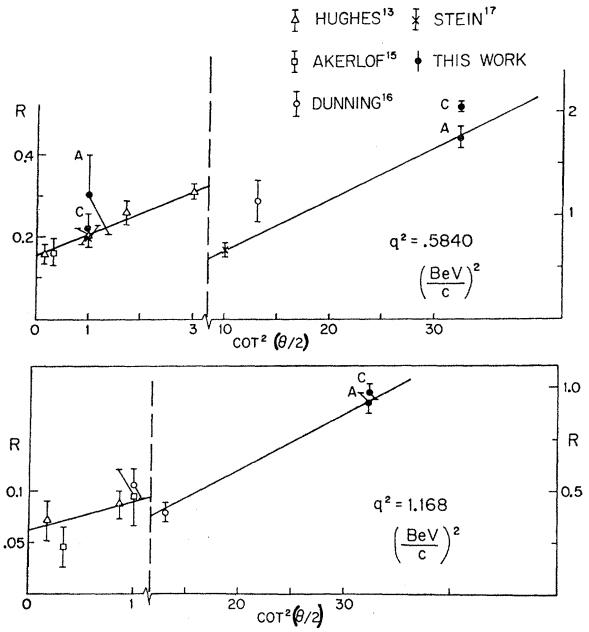

FIG. 43. Plots of $R=\sigma_{\text{neutron}}/[\sigma_{\text{Mott}}\times(E/E')\times\tan(\frac{1}{2}\theta)\times(1+\tau)^{-1}]$ for $q^2=0.5840$ and 1.168 (BeV/c)^2 to show method of extracting form factors. C=coincidence method data; A=area-method data.

[44] G. F. Chew and F. E. Low, Phys. Rev. **113**, 1640 (1959).

in the same fashion is currently in progress by members of our Harvard group, and preliminary results are encouraging.

The basic reasoning in the extrapolation procedure is as follows. We write the scattering amplitude as

$$f=D/(E_s+\tfrac{1}{2}\epsilon)+F,$$

where ϵ is the deuteron binding energy and E_s the energy of the spectator neutron. The first term is the impulse approximation term in which the fastly varying kinematic dependance due to the pole at $E_s=-\frac{1}{2}\epsilon$ has been made explicit, leaving the function D which is a more slowly varying function of the proton angles and energies. The term F is a final-state correction term, which is expected to be small by comparison with D, and is also a slowly varying function of the angles and energies. The cross section is then given by

$$\frac{d^3\sigma}{dE'd\Omega d\Omega_p}=|f|^2=\frac{D^2}{(E_s+\frac{1}{2}\epsilon)^2}+\frac{2\,\mathrm{Re}(F^*D)}{E_s+\frac{1}{2}\epsilon}+F^2.$$

Provided that F is indeed small, the measured cross section is dominated by the first two terms, the second of which may easily be negative, as was the case in p-d scattering and seems to be the case for e-d scattering.

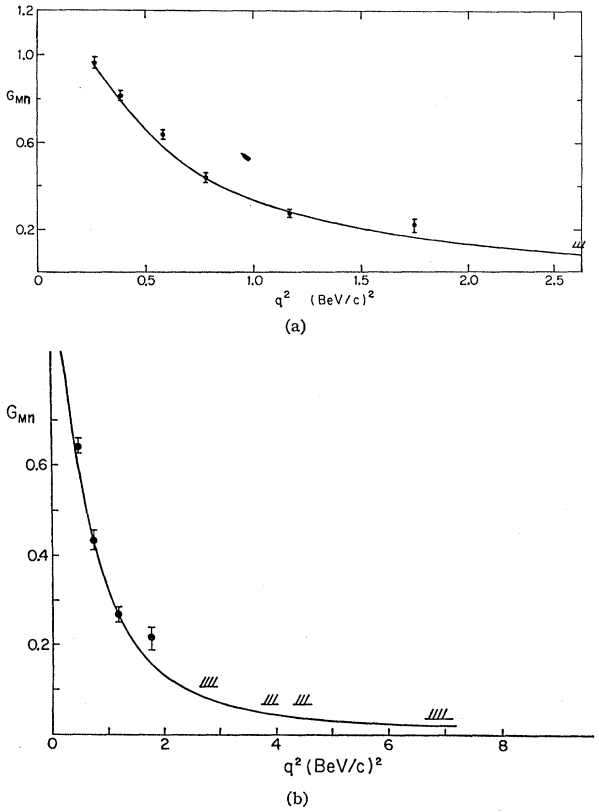

FIG. 44. $G_{Mn}(q^2)$ versus q^2, a least-squares fit. (a) $q^2=0$ to 2.725 (BeV/c)^2. (b) $q^2=0$ to 6.814 (BeV/c)^2. Upper limits [above 2 (BeV/c)^2] are 2-standard-deviation limits from Table XIII. Line is the dipole fit.

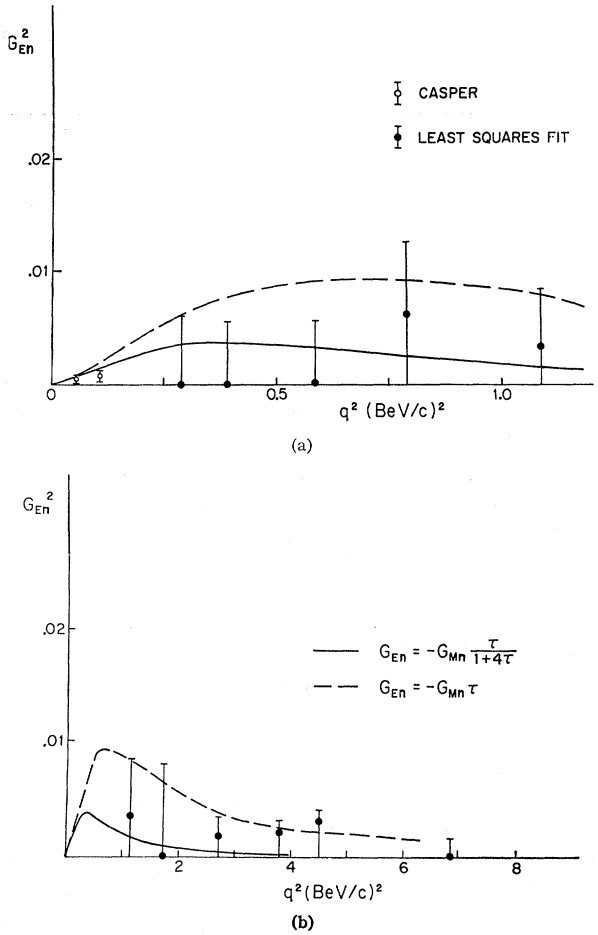

FIG. 45. $G_{En}(q^2)$ versus q^2, a least-squares fit. (a) $q^2=0$ to 1.186 (BeV/c)^2. (b) $q^2=0$ to 6.814 (BeV/c)^2. Upper limits assume G_{Mn} given by the dipole fit. The limits would be about two standard deviations higher if no assumption is made concerning G_{Mn}. The dashed line is the prediction of $G_{En}=-\tau G_{Mn}$, while the solid line results from assuming $G_{En}=[-\tau/(1+\tau)]G_{Mn}$. In both these cases the "dipole fit" has been used for G_{Mn}.

In integrating over recoil proton angles ($d\Omega_p$) to obtain the noncoincidence cross sections, the interference term is expected to vanish, as can be seen from a closure argument.[45] We can understand the lower differential cross sections, then, in terms of protons scattered outside of the recoil-proton detector.

We suggest that a complete theory of final-state interactions, developed along the lines sketched above, may justify the noncoincidence data rather than the peak-method or the coincidence data, in spite of the arguments of pole models and contrary to our own preconceptions.

In the spirit of the above discussion, we suggest that the discrepancy between the σ_n/σ_p results of the area and coincidence methods may provide a reasonably conservative estimate of the theoretical errors in the de-

[45] G. F. Chew, Phys. Rev. **80**, 710 (1951); R. L. Gluckstern and H. A. Bethe, *ibid.* **81**, 761 (1951).

TABLE XIII. Values for G_{Mn} derived from data of Refs. 13, 15, 16, 17 and area method data of the present work.

q^2 (F^{-2})	q^2 $(BeV/c)^2$	Least-squares fits to: All data[a]	Least-squares fits to: $\theta_e \geq 90°$ data[a]	Systematic[b] error	Phenomenological fits: Dipole fit	Phenomenological fits: Scaling law
7.5	0.2920	0.964 ± 0.023	1.02 ± 0.035	$+0.039, -0.045$	0.9600	0.915 ± 0.02
10	0.3894	0.812 ± 0.020	0.831 ± 0.035	$+0.040, -0.043$	0.7975	0.765 ± 0.02
15	0.5840	0.637 ± 0.019	0.618 ± 0.038	$+0.027, -0.029$	0.5756	0.575 ± 0.02
20	0.7784	0.435 ± 0.022	$0.506_{-0.044}^{+0.041}$	$+0.023, -0.047$	0.4349	0.445 ± 0.015
30	1.168	$0.267_{-0.021}^{+0.017}$	$0.231_{-0.052}^{+0.043}$	$+0.014, -0.016$	0.2733	0.280 ± 0.006
45	1.752	$0.220_{-0.033}^{+0.029}$	...	± 0.006	0.1590	0.165 ± 0.005
70	2.752	0.093[c] (0.111)	...	± 0.003	0.0816	0.085 ± 0.004
100[d]	3.894	0.060[c] (0.068)	...	± 0.002	0.0455	0.047 ± 0.003
115	4.478	0.056[c] (0.066)	...	± 0.002	0.0358	0.037 ± 0.002
175[d]	6.814	0.016[c] (0.032)	...	± 0.001	0.0170	0.017 ± 0.001

[a] Error includes only experimental uncertainties in the sense of a standard deviation.
[b] Systematic error obtained by varying $\sigma_{ep} \pm 5\%$ and redetermining $\sigma_{en} = \sigma_{ed} - \sigma_{ep}$.
[c] Upper limits computed by assigning entire cross section to G_{Mn}^2. Numbers in parentheses are two standard-deviation limits (from Ref. 16).
[d] From Ref. 16.

termination of σ_n/σ_p. The discrepancy between $\sigma_{p\mathrm{D}}$ and $\sigma_{p\mathrm{H}}$ may also be taken as an estimate of the uncertainty in the determination of the noncoincidence-area-method cross section. This leads to a very similar uncertainty in σ_n/σ_p.

(c) In the third approach, we consider the most general recoil-proton angular distribution which can arise if only one-photon exchange occurs. It is

$$A(\theta)+B(\theta)\cos\phi+C(\theta)\cos(2\phi),$$

where θ and ϕ are the polar and azimuthal angles with respect to the momentum-transfer (virtual-photon) direction. There is no term which would lead to an up/down asymmetry and we therefore believe that the one datum point which shows such an asymmetry (see Fig. 40) must be spurious. The term $A(\theta)$ is the sum of the squares of longitudinal and of transverse photon amplitudes. We observe a slightly narrower distribution than we predicted by the theory in the absence of final-state interactions. The term $[B(\theta)\cos\phi]$ is due to interference between excitation by longitudinal and by transverse photons, and gives rise to a left/right asymmetry. We see such an asymmetry at only one point (at 10 F^{-2} above the peak) and, since it is associated with the previously mentioned up/down asymmetry, which is probably spurious, we believe that it too may not be genuine. We know of no calculations which could give rise to such an interference term as a result of final-state interactions. The term $[C(\theta)\cos(2\phi)]$ is due to a transverse-transverse interference term arising from linear polarization of the electromagnetic field. Such a term gives rise to the asymmetry of the proton angular distribution observed in photodisintegration of the deuteron. At 100 MeV (approximately equivalent to the energy transfer at 5 F^{-2}) this asymmetry is about $0.3\sin\theta$, where θ is the polar angle measured in the center-of-mass system of the final n and p. We have not made a detailed analysis of the angular distributions but our data do not contain a significant $\cos(2\phi)$ contribution.

XIV. REVIEW OF NEUTRON FORM FACTORS

The tenor of the previous sections has, in large part, been that the existing deuteron theories are inadequate to explain the experimental results. It is therefore hard to extract neutron form factors from these data with a reliability approaching the experimental precision. Neutron form factors extracted from all previous experiments probably have similar problems and errors. Our improved experimental precision has merely emphasized the problems. This section discusses our present best knowledge about the neutron form factors.

We note first that coincidence electron-proton data from the deuteron give smaller cross sections than originally expected; a possible reason for this has been discussed in Sec. XIII, where comparisons were made with inelastic proton-deuteron scattering. We noted in Fig. 34 that above $q^2 = 10$ F^{-2} the discrepancy was approximately 5% in $\sigma_{p\mathrm{D}}/\sigma_{p\mathrm{H}}$. We shall take this as an estimate of the error in the interpretation of area method electron-deuteron cross sections in this paper and in the papers of others.

To extract neutron form factors, we have used data on inelastic electron scattering from five sources. Hughes *et al.*,[13] Akerlof *et al.*,[15] Dunning *et al.*,[16] and Stein *et al.*,[17] supplement the *noncoincidence* data of this work. All but Stein *et al.* measured σ_{ed}/σ_{ep} ratios. The values of σ_{ep} used here employ the latest information on proton form factors,[5,46–48] the errors of which are typically $\frac{1}{3}$–$\frac{1}{4}$ of the other errors. σ_{en} is derived from $\sigma_{en} = \sigma_{ed} - \sigma_{ep}$. The theoretical errors in this relation are approximately 5% in the e-d cross section and therefore 15–30% in the e-n cross section. This error is common to all points and was not included in the fitting program. We have inter-

[46] T. Janssens, E. Hughes, M. Yearian, and R. Hofstadter, Phys. Rev. **142**, 922 (1966); P. Lehmann, R. Taylor, and R. Wilson, *ibid.* **126**, 1182 (1962).
[47] H. Behrend, F. Brasse, J. Engler, H. Hultschig, S. Galster, G. Hartwig, H. Schopper, and E. Ganssauge, Nuovo Cimento **48**, 140 (1967); W. Albrecht, H. Behrend, H. Dorner, W. Flauger, and H. Hultschig, Phys. Rev. Letters **18**, 1014 (1967).
[48] M. Goitein, J. R. Dunning, Jr., and Richard Wilson, Phys. Rev. Letters **18**, 1018 (1967).

TABLE XIV. Values for G_{En}^2 using least-squares fit to all the data (excluding our coincidence measurements). Numbers in parentheses are two-standard-deviation limits.

q^2 (F^{-2})	q^2 (BeV/c)^2	Least-squares fits to all data[a]	Systematic error[b]	Phenomenological fits[c] $G_{En}=-\tau G_{Mn}$	$G_{En}=-[\tau/(1+4\tau)]G_{Mn}$
7.5	0.2920	Zero ±0.0065 (−0.0054)	+0.015, −0.011	0.00633	0.00357
10	0.3894	Zero ±0.0062 (−0.0066)	±0.009	0.00776	0.00373
15	0.5840	Zero ±0.0055 (−0.0159)	±0.005	0.00910	0.00329
20	0.7784	0.0062±0.0066	+0.002, −0.0025	0.00924	0.00260
30	1.168	0.0034±0.0050	±0.0011	0.00821	0.00152
45	1.752	Zero ±0.008 (−0.011)	±0.008	0.00625	0.00070
		Assumption[e]			
		A	B		
70	2.752	≤0.0074 (0.0088)	≤0.0016 (0.0048)	0.00398	0.00024
100[d]	3.894	0.0051 (0.0068)	0.0021 (0.0041)	0.00253	0.00009
115	4.478	0.0052 (0.0075)	0.003 (0.005)	0.00207	0.00006
175[d]	6.814	0.00094 (0.0037)	Zero (0.0028)	0.00108	0.00001

[a] Experimental errors only—one standard deviation.
[b] Same procedure followed as with G_{Mn}.
[c] Dipole fit used for G_{Mn}.
[d] From Ref. 16.
[e] Assumption A: entire cross section assigned to G_{En}^2. Assumption B: dipole fit used to calculate G_{Mn}^2 contributions.

polated data to the same momentum transfer where appropriate; it is well known[20] that such interpolations introduce a negligible error. In Fig. 43 are presented "Rosenbluth" plots[20] of the cross section versus $\cot^2(\frac{1}{2}\theta)$ at two momentum transfers.

A least-squares fit was performed at all q^2 where three or more data points were available. The χ^2 for these fits ranged from 1.1 to 0.7 per degree of freedom. The results for G_{Mn} are listed in Table XIII, and are shown in Fig. 44.

For low momentum transfers, less than 1 (BeV/c)^2, G_{Mn} can be obtained from large-angle data independent of G_{En}, providing G_{En} is small (which it is). However, it can be seen in Table XIII that G_{Mn} is independent of whether or not the small-angle data are included. At the highest momentum transfers only upper limits are available; these are included because they are useful in excluding some theoretical models of form factors.

We note that the form

$$\frac{G_{Mn}(q^2)}{\mu_n}=\frac{G_{Mp}(q^2)}{\mu_p},$$

(the so-called "scaling law") agrees with the data to within the errors of 5–8% in the neutron magnetic form factor. We also note that, to within the limited error, G_{Mn} is given by the "dipole" fit $G_{Mn}(q^2)=\mu_n/[1+(q^2/0.71)]^2$ as shown in Fig. 44.

$G_{En}(q^2)$ is more difficult to obtain because it only contributes small fractional amounts to the electron-neutron cross section and still smaller amounts to the electron-deuteron cross section. G_{En}^2 was derived from the same plots (Fig. 43) used to derive G_{Mn}^2. When G_{En}^2, so derived, becomes negative, we put it equal to zero with the same error. Figure 45 and Table XIV show the situation. The dashed line is a form $G_{En}=-\tau G_{Mn}$ which is an extrapolation suggested by the *slope*,[8] $dG_{En}/(dq^2)$, measured near $q^2=0$. The form is not inconsistent with the least-squares separation. However, if the "dipole" fit is assumed and the comparison is made directly to the ratio, σ_n/σ_p, as in Fig. 34, then the form $G_{En}=-\tau G_{Mn}$ is actually excluded by the higher-q^2 data. Also, we consider it "unreasonable" in the sense that it predicts $G_{En}\gg G_{Mn}$ for sufficiently large q^2.

The solid line is a form $G_{En}=-[\tau/(1+4\tau)]G_{Mn}$ which approximately satisfies the low-energy electron-neutron interaction and has a "reasonable" behavior as $\tau\rightarrow\infty$.

The low-momentum-transfer values are those evaluated by Casper and Gross[11] from elastic e-d scattering data using the Feshbach-Lomon deuteron wave functions. These points would each be about one standard deviation lower if the Hamada-Johnston wave function were used.

We note that if we had used our "coincidence" data, abnormally large values of G_{En} would result if only experimental errors are considered. However, the errors indicated in Fig. 34 are purely experimental and take no account of the theoretical uncertainties involved in interpreting the coincidence data in terms of the free electron-neutron cross sections.

Finally, it is worth emphasizing that, while the form factors as shown herein are expected to be correct within their very considerable errors, if a specific theoretical

model of form factors is to be tested, it is best to compare directly with plots of σ_n/σ_p such as are given in Figs. 27–34.

ACKNOWLEDGMENTS

The authors wish to thank the Harvard Cyclotron staff and shops and the Cambridge Electron Accelerator Staff for their valuable assistance throughout all phases of the experiment. Professor Norman Ramsey aided in the initial setup of the experiment. The experiment would not have been possible without the use of a PDP-1 computer under the direction of Dr. A. Brenner. Dr. I. McGee helped to provide insight into some of the theoretical problems. J. Alberi, G. Gladding, A. Liberman, A. Litke, and G. Thomson helped in the preparation of the apparatus and during data taking. Part of the data analysis done at the Harvard Computation Center was funded by the National Science Foundation under Grant No. GP-2723.